DESIGN AND OPTIMIZATION OF A LIQUID BIOPSY COLLECTOR FOR OVARIAN AND ENDOMETRIAL CANCER SCREENING

by

PAOLA ULACIA FLORES

DEPARTMENT OF MECHANICAL ENGINEERING
MCGILL UNIVERSITY, MONTREAL

APRIL 2020

A thesis submitted to McGill University in partial fulfillment of the requirements of the degree of Master of Engineering

ABSTRACT

Ovarian and endometrial cancers are among the leading causes of death for women over 45 years of age in developed countries, and the deadliest of gynecological cancers with an overall survival rate of 46.5%. Every year, 15,000 women die in the US and Canada of this disease.

Currently there is no screening program in place, and the diagnostic tools available are neither specific nor sensitive enough for early detection. The standard of care is relevant in assessing and staging previously diagnosed cancer but has not proven effective for early detection.

Dr. Gilbert's research group at the McGill University Health Centre (MUHC) has developed a test to detect these cancers early, based on the identification of genetic tumoral markers from intrauterine samples; however, the tools they had available for procuring these samples were not ideal; For this, we set out to design a collector for liquid biopsies from the uterine cavity.

Design methodologies for manufacturability were used to obtain the first generation of the intrauterine liquid biopsy sampler. Verification and validation *in vitro* tests were performed throughout the process for structural stability, volumetric collection performance and ease of use.

The new designs showed an increase in volume collection of 1.3 times when compared to the control and transferred 1.4 times as much sample to the preservation vial. The devices were structurally sound and safe to use under normal conditions.

RESUMÉ

Les cancers de l'ovaire et de l'endomètre sont parmi les principales causes de décès des femmes de plus de 45 ans dans les pays développés et les plus meurtriers des cancers gynécologiques avec un taux de survie global de 46,5%. Chaque année, 15 000 femmes meurent aux États-Unis et au Canada de cette maladie.

Actuellement, aucun programme de dépistage n'est en place et les outils de diagnostic disponibles ne sont ni spécifiques ni suffisamment sensibles pour une détection précoce. Les soins standards permettent d'évaluer et d'établir le stade d'un cancer précédemment diagnostiqué, mais n'a pas été prouvé efficace pour la détection précoce.

Le groupe de recherche du Dr Gilbert du Centre Universitaire de Santé McGill (CUSM) a mis au point un test de détection précoce de ces cancers, basé sur l'identification de marqueurs tumoraux génétiques à partir d'échantillons intra-utérins. Cependant, les outils dont il disposa pour se procurer ces échantillons n'étaient pas idéaux, nous avons donc décidé de concevoir un échantillonneur pour biopsies liquides de la cavité utérine.

Des méthodologies de conception pour la fabricabilité ont été utilisées pour obtenir la première génération de l'échantillonneur de biopsie liquide intra-utérine. Des tests de vérification et de validation *in vitro* ont été effectués tout au long du processus pour la stabilité structurelle, les performances de collecte volumétrique et la facilité d'utilisation.

Les nouveaux concepts ont montré une augmentation du volume de collecte de 1,3 fois par rapport au contrôle et ont transféré 1,4 échantillons de plus dans le flacon de conservation. Les appareils sont structurellement solides et sûrs à utiliser dans des conditions normales.

For Julia, may my attempts to show you by doing inspire you to pursue your wildest dreams and make them happen.

ACKNOWLEDGEMENTS

I would like to express my sincere gratitude to my advisors, Prof. Rosaire Mongrain and Prof. Lucy Gilbert, for the continuous support and guidance during my studies and research. Their patience, motivation and attention to detail helped me greatly throughout my research as well as the process of writing this thesis. Lucy, thank you for trusting me and giving me the opportunity to work on this project, your motivation, drive and perspective on the end-goal kept me going when I felt most lost and overwhelmed.

I would also like to thank the DOvEE research team at the CIM-MUHC, particularly Dr. Claudia Martins, Taylor Grant, Alicia Schiavi and Lawrie Shahbazian, for their help navigating the hospital and coordinating resources.

My sincere thanks also go to Ms. Valerie Aitkens not only for her generous contributions for Cancer Research, but also for welcoming me into her home, her continuous interest and encouragement in the process.

I'd like to thank Dr. Ramses Galaz and the GSE Biomedical team for their assistance in the manufacturing of prototypes and continuous support to develop and help perfecting our ideas.

I thank my friends and fellow lab mates at McGill University: Andrea Sanchez, Christopher Zikry, Pooya Tavakoli, Raphael Limbourg, Stanislas Le Guisquet, Ahmed Abdelaziz, Jamil El Najjar, Ahmed Bayoumi, and Osaid Matar for the stimulating discussions, encouragement and help understanding new concepts, providing much needed feedback at times, and for making life a bit more fun in the last two years.

To my family and friends around the globe, who push me to face new challenges, and have helped me stay focused through high and low. I wouldn't have made it without your support.

TABLE OF CONTENTS

LIST OF FIGURES

LIST OF TABLES

LIST OF TERMS AND ABBREVIATIONS

ACOG	American Congress of Obstetricians and Gynaecology
CA-125	cancer antigen 125
CC	critical component
CNR	Contrast-to-noise ratio
CRI	Cervical resistance index
CT	Computed tomography
CTC	Circulating tumor cell
ctDNA	Cell-free circulating DNA
Curette	A surgical instrument used to remove material by a scraping action
DALY	Disability-adjusted life years
DNA	Deoxyribonucleic acid
DOVEE	Detecting Ovarian and Endometrial cancers Early
ECM	Extracellular matrix
EDCA	Endometrial cancer
EMI	Endometrial-myometrial interface or junctional zone
FAST	Functional analysis system technique
FIGO	International Federation of Gynecology and Obstetrics
Fr	French, refers to catheter size standards 3 Fr = 1mm
FRFSE	Fast Recovery Fast Spin Echo is a pulse sequence used in MR
IUF	Intrauterine fluid
Mesothelium	Tissue that lines the great cavities of the body
MMS	Multimodal screening, including CA125 and TVUS
MNR	Magnetic nuclear resonance

MR	Magnetic resonance
MUHC	McGill University Health Centre
NCC	Non-critical component
Ova	Female germ cells
OVCA	Ovarian cancer
OVECA	Ovarian and endometrial cancers
PEBAX	Polyether block amide
PFD	Pelvic floor disorder
PVA	Polyvinyl alcohol
QALY	Quality-adjusted life years
RI-MUHC	Research Institute, McGill University Health Centre
SMC	Smooth muscle cells
SNR	Signal to noise ratio
STL	Stereolithography file extension
Stroma	From Latin *stromat* - (bed), in anatomy, it refers to the tissue providing support to an organ
TNM	Tumour, Node, Metastasis staging system, where T stands for tumor size, N to the nearby lymph nodes with cancer and M to whether the cancer has metastasized or not.
TPU	Thermoplastic urethane
TVUS	Transvaginal ultrasound
UV	Ultraviolet
UKCTOCS	United Kingdom Collaborative Trial of Ovarian Cancer Screening
WHO	World Health Organization

1 INTRODUCTION

1.1 RATIONALE

Ovarian cancer (OVCA) is the 5th leading cause of cancer deaths in women, and the deadliest of any gynecological cancer with an overall survival rate of 46.5%[1]–[4]. According to the Canadian Cancer Society, in 2018 there were approximately 2,800 new cases diagnosed and 1,800 deaths caused by ovarian cancer [4]. This trend is comparable to USA statistics, where in 2017 there were an estimate of 14,080 deaths, accounting for 2.3% of all cancer deaths[2]. The disease typically presents asymptomatically and is only detected at a late stage, when the 5-year relative survival rate is only about 29%, with an overall survival rate of 46.5%[3].

Endometrial cancer (EDCA) is the 6th leading cause of cancer deaths in women, the most common malignancy of the female genital tract in developed countries, and the 4th most common cancer in women in the USA and Canada[5], accounting for 7% of all new cancer diagnoses in women[6],[7]. The Canadian Cancer Society estimates 7,200 new cases of EDCA in 2019, with a total of 1,250 deaths from the disease[8]. In the USA, the American Cancer Society estimates about 61,880 new cases of EDCA and 12,260 deaths in 2019[9], accounting for 2% of all cancer deaths [10]. If detected early, EDCA presents with a 5-year relative survival rate of up to 95%, however, if detected at a later stage it drops significantly to 16% [11]. The overall survival rate is 69% [12].

Together, OVCA and EDCA accounted for 8.2% of all new female cancer cases in 2018, and 7% of cancer related deaths for females aged 45 or more[13]. According to the WHO[14], in 2004 there was a total of 24,000 DALYs[1] lost due to ovarian and endometrial cancer in Canada alone.

[1] DALY: Disability-Adjusted Life Year (Years of Life Lost + Years Lost to Disability)—1 DALY equals to 1 lost year of healthy life

While medicine has greatly improved in pharmacological treatment for different types of cancer, not much has changed in the past few decades in screening and detection for ovarian and endometrial cancer, which has led to relatively steady mortality rates.

Currently, the standard of care for assessing pelvic masses includes a pelvic exam followed by tumoral marker tests, imaging and, if deemed necessary, an endometrial biopsy. These methods have proven to be unspecific for the early detection and are highly dependent on the ability of the healthcare professional to take a sample of the area of interest during a biopsy.

The United Kingdom Collaborative Trial of Ovarian Cancer Screening (UKTOCS) assessed the cost-effectiveness of a multimodal screening (MMS) approach which includes CA-125 tests and transvaginal ultrasound (TVUS), against the effects of no screening. This study found that MMS achieved an incremental 0.47 QALYs[2][15], and concluded that a screening program for OVCA could potentially reduce mortality by 15%, although there is currently still no evidence-proven screening method for OVCA[16].

Several groups, including Dr. Gilbert's group at the MUHC, are currently working on identifying and detecting pathogenic somatic mutations associated with ovarian and endometrial cancers in biofluids[17]–[20], for the development of an early detection test. These new methods have shown to detect EDCA and OVCA in cervical pap samples, with higher detection rates closer to the source of the disease, i.e. the endometrium and the ovaries[20].

However, currently available biopsy devices are not designed for the collection of biofluids from the uterine cavity or tubes, but rather to obtain a piece of tissue for a histopathologic analysis, leaving a gap for the development of new medical devices.

The goals of this work are to assess and refine the design of a liquid biopsy sampler for ovarian and endometrial cancer screening, as well as adequate verification and validation methods for the *in-vitro* testing of these devices.

---

[2] QALY: Quality-Adjusted Life Year — Refers to years of healthy life gained

1.2 OBJECTIVES

The specific objectives of this work are:

1) To design and optimize a device for the acquisition of liquid biopsy samples from the uterine cavity based on the pathophysiology of ovarian and endometrial cancers and the biomechanical properties of the affected tissues.
2) To develop *in vitro* testing methodologies for its verification and validation
    a. To assess the structural integrity (strength) of such a device through mechanical testing (uniaxial tensile and compressive testing).
    b. To evaluate its *in vitro* performance (efficiency) through volume collection and spectrophotometry methods.
    c. To assess the feasibility of the creation of an anatomically and mechanically representative model for *in vitro* testing of gynecological devices through image segmentation and additive manufacturing techniques.

2 BIOMEDICAL BACKGROUND

This section presents the structure of the female internal genital organs, linking the anatomy and structure to function and building towards understanding the pathophysiology of gynecological cancers, and their diagnostic and therapeutic tools. The link between structure and function will be studied further in the context of the biomechanical properties of these tissues.

2.1 THE FEMALE GENITAL TRACT

The female genital organs are located within the pelvic cavity, they are a series of interconnected organs that work together towards the main sexual and reproductive functions, as well as hormone production and secretion. The uterus connects to the exterior of the body through the cervix and the vagina, and to the peritoneum and the ovaries through the oviducts.

2.1.1 FUNCTIONAL ANATOMY OF THE FEMALE GENITAL TRACT

The ovaries – The ovaries are oval shaped, measure approximately 4 × 2 cm and connect to the uterine cavity through the uterine tubes. They are attached at the uterine horns (*cornua*) by the ovarian ligaments and are covered by a single-cell layer, the ovarian (germinal) epithelium; which is continuous with the mesothelium[3] of the peritoneum and encases the fibrous stroma[4] containing the germ cells (oocytes).

The uterine (Fallopian) tubes – The uterine tubes present bilaterally and extend from the uterine *cornua* to the peritoneal cavity close to the ovaries. They are approximately 10 cm long and can be divided in four portions with variable inner diameters. The intramural portion connects to the uterine cavity by penetrating the myometrium at the *cornua*; the isthmus, 2 to 3 cm long, is the narrowest portion of the tube with a lumen diameter of 1 mm, which increases to close to 1 cm as it reaches the widest part at the ampulla; the oviduct ends at the infundibulum,

[3] *Mesothelium* – Tissue that lines the great cavities of the body.

[4] *Stroma:* from Latin *stromat-* (bed), in anatomy, it refers to the tissue providing support to an organ.

the distal most portion of the tube, fringed by fimbriae which come in contact with the ovary. The infundibulum opens into the peritoneum and is connected to the exterior of the body through the vagina. Recent evidence suggests most high-grade serous ovarian cancer originates in the oviducts.[21]

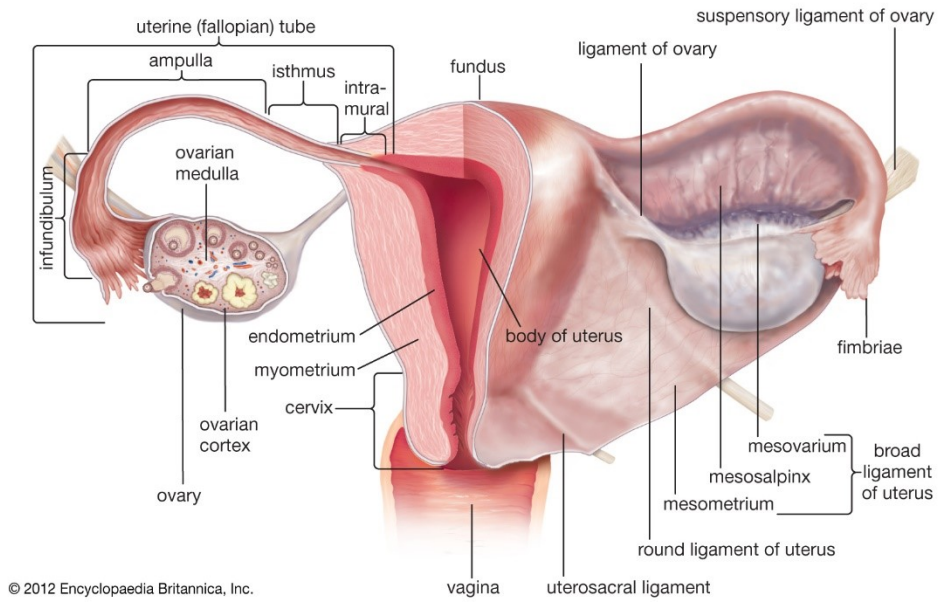

Figure 2-1 — Frontal view and cross section of the internal genital organs; reproduced with permission from [22].

The uterus – The inverted pear-shaped uterus measures about 7 × 4 cm and consists of a fundus, the *cornua*, a body, and a cervix. It is located between the bladder and the rectum. The uterus is comprised of three layers: the endometrium lines the uterine cavity and has a superficial mucous functional layer; the myometrium is made up of two layers of smooth muscle cells embedded in connective tissue and is responsible for the contractions essential in childbirth; and the outermost layer, the perimetrium, encases the organ.

The cervix – The cervix connects the uterus and vagina and projects into the upper vagina. The cervix is about 2.5-cm long with a fusiform endocervical canal lined by columnar epithelium lying between an internal and external *ora* or openings, 1 to 2.5 mm and 2.5 to 4 mm in diameter respectively.

The vagina – The vagina is an elastic fibromuscular tube opening from the cervix, passing through the perineal membrane, and it forms a 90- to 170-degree angle against the body of the uterus. The cervix opens into the posterior vaginal wall, bulging into the vaginal lumen[23].

The peritoneum – The peritoneum is a protective layer lining the abdominal and pelvic cavities. It is formed by a single layer of squamous cells over a thin sheet of connective tissue and covers the organs to protect them from friction between one another[21],[23][24].

The female genital tract is filled with fluids of different compositions and functions along its different zones, aiding in the transport of sperm and oocytes primarily. Their properties respond to changes in hormonal stimulation with varied protein and biochemical compositions resulting in increased or reduced viscosity and fluid properties related to their individual functions[25]–[31]. These fluids take the name of their anatomical location; intrauterine fluid (IUF) in the uterine cavity[32]; and cervical or oviduct mucus in the cervix and oviducts respectively; vaginal fluids are produced by glands at the cervical vestibule[20],[33],[34].

2.1.2 WALL STRUCTURE OF THE FEMALE GENITAL TRACT

The female genital tract, like most biological tissues and hollow viscera, is built with a hierarchical structure comprised of an inner mucosa serosa, a medial muscularis and an outer serosa; which in turn are built of cellular and fibrillar structures[35]. We will see this organization repeats throughout the different structures of the tract, with characteristics specific to each organ.

In the uterus, these three main layers are the endometrium, the myometrium and the perimetrium (Figure 2-2)[23],[34]. The innermost layer of the uterus, the endometrium, grows during the menstrual cycle to prepare for the implantation of an embryo and sheds if no implantation has occurred, causing the menstrual bleeding. The endometrium is also considered a functional endothelium due to its role in the secretion of the intracavity fluids, aiding in the adequate functioning of the organ[36].

The myometrium, or middle layer, is mostly formed by smooth muscle cells (SMC), collagen and elastin fibres. The SMC assemble in bundles, embedded in a sponge-like matrix of elastin and collagen; its ultrastructure has been identified by histological and microimaging methods, and shows three differentiated layers or stratums, with SMC bundles running in a circumferential or spiral pattern (*stratum vasculare*); and longitudinally (*stratum subvasculare*) or obliquely (*stratum supravasculare*) along the long axis of the uterus,[34][37] resembling the arrangement of fibres in the arterial media. These orientations and characteristics provide the organ with expansive and compressive properties [34]. The interface between endometrium and

myometrium (EMI) is called the junctional zone, and is where the secretory functional endothelium resides, playing a key role in normal reproduction, as well as the development of pathologies. The myometrium is continuous with the muscular layer of the uterine tubes and the vagina[37]. The perimetrium, or outermost layer, is mostly made of loose connective tissue, and provides protection against friction with surrounding organs.

The cervix, connecting to the uterine cavity and the vagina through the internal and external *os* respectively, gradually transitions from the muscular structure of the uterus, to the elastic, collagenous cervical tissue[38]–[41]. The extracellular matrix (ECM) is composed of a dense network of cross-linked type I and III collagen fibres with longitudinal and circumferential orientations embedded in a mix of glycosaminoglycans and proteoglycans[34] [42] (Figure 2-2); together with bundles of SMC in a longitudinal and circumferential pattern preserved from the uterus[35],[37], provide the cervix with its load-bearing properties and allow for force transmission and signaling mechanisms between the structures[34].

The cervix acts as a mechanical barrier to the uterine cavity. Its load-bearing component, the stroma, undergoes remodelling during pregnancy to allow for the expulsion of the fetus during labour.[39]

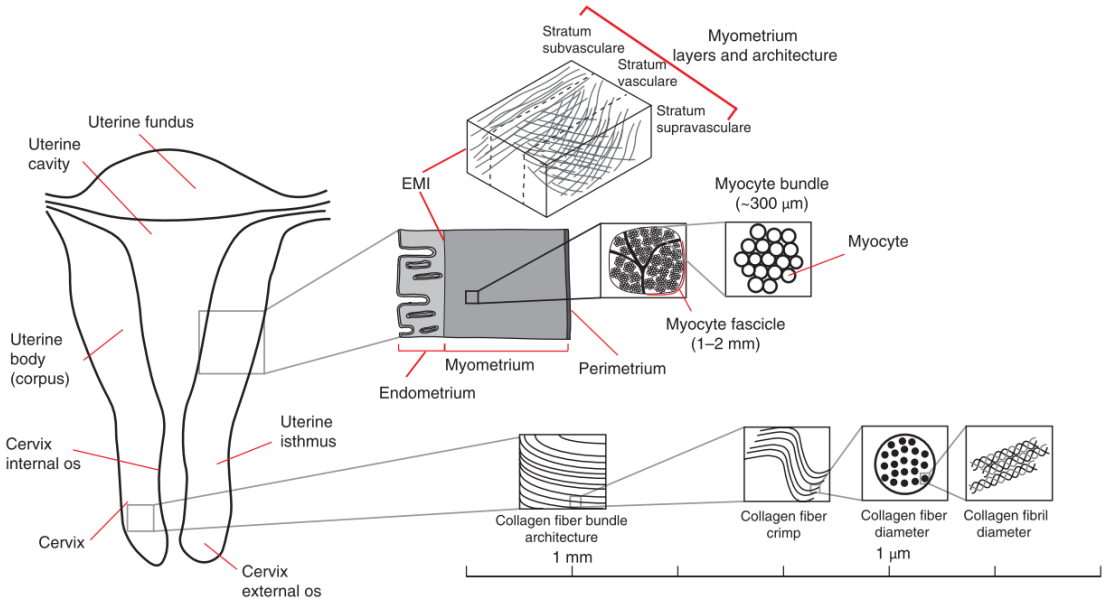

Figure 2-2 — The oblique frontal cross section of the human uterus. Uterine and cervical function is dictated by its hierarchical smooth muscle cell (SMC, i.e., myocyte) and collagen fiber structures at various biological length scales. Reproduced with permission from [34].

The oviduct wall, like the uterus and other hollow organs, presents with an inner mucosa, an intermediate muscular layer, and an outermost serosa or peritoneum.

The *tubal muscularis* is a continuation of the uterine myometrium and is organized in an inner thick circular layer and a thinner outer longitudinal layer of SMC bundles. The mucosa forms folds and is lined by a simple columnar epithelium with ciliated and non-ciliated secretory cells, which aid in the transportation of particles within the tubes and produce a nutritive fluid for the ovum, respectively[37][44].

The vaginal wall has a structure similar to that of the uterus and the uterine tubes with the addition of a highly vascularized elastic layer, the *lamina propria*, also considered a submucosa; which together with the inner adventitia contributes to the elasticity and strength of the vaginal wall.

All tissues are surrounded by an ECM, which provides a support network for cells and tissues, amongst other functions [35],[45],[46]. It contains a variety of proteins, proteoglycans, and glycoproteins that are arranged in different configurations to create fibrils, like collagen and elastin, or other structures. These configurations provide biological tissues with specific mechanical properties [45]–[47].

Collagen is a protein fibre with a triple-helical conformation and over 25 different types[41]. It provides structure to cells and is the major component of fibrous tissues. Elastin, another protein of the ECM, is a cross-linked elastic fibre, organized in a three-dimensional network, it allows tissues to stretch and distend[35],[47]. These fibres are interwoven with each other in different proportions and greatly determine tissues' mechanical properties, which will be further described in Chapter 3.

2.2 CLINICAL AND EPIDEMIOLOGICAL CONSIDERATIONS: OVARIAN AND ENDOMETRIAL CANCER

Ovarian and endometrial cancers (OVECA), although different in origin and affected structures, share similar age-specific incidence curves, risk factors, signs and symptoms as well as diagnostic and therapeutic options. For this reason, we present them together. This section will discuss the epidemiology and pathophysiology of OVCA and EDCA and will look deeper into the available diagnostic options.

2.2.1 EPIDEMIOLOGY AND PATHOPHYSIOLOGY

Ovarian cancers include tubal and peritoneal cancers, while endometrial cancer refers to cancers occurring in the body of the uterus, together with uterine sarcomas and placental cancer. Ovarian and endometrial cancers are the most common of them with a worldwide age-adjusted incidence rate[5] of 6.6 and 8.4, respectively;, and 8.4 and 20.5 in North America[13].

Table 2-1 — Age-adjusted incidence rates for OVECA in different regions of the world[6].

Region	Incidence				Mortality			
	All ages		45 +		All ages		45 +	
	EDCA	OVCA	EDCA	OVCA	EDCA	OVCA	EDCA	OVCA
World	8.4	6.6	29.1	19.3	1.8	3.9	6.6	13.2
Developed regions	16.7	8.6	58.9	26.3	2.7	4.3	9.9	15.2
North America	**20.5**	**8.4**	**73.1**	**26.8**	**3.0**	**4.1**	**11.1**	**14.8**
USA	20.1	8.5	71.6	27.1	3.0	4.1	11.2	14.7
Canada	23.6	7.9	85.5	24.7	2.7	4.4	10.3	15.9

Together, OVCA and EDCA accounted for 8.2% of all new female cancer cases in 2018, and 7% of cancer-related deaths for females aged 45 or more [13]. Worldwide, they represent an estimated 619,000 new cases and 242,000 deaths annually. Mortality rates are high because more than 70% of women with ovarian cancer are diagnosed at advanced stages, when the five-year

[5] Age-adjusted rates per 100,000 standardized to world population

[6] Age-Adjusted Rates are per 100,000 and are adjusted to the World Standard. [6]

survival rate is only 29% [48]. For endometrial cancer, the survival rate drops from 95% to 16% at later stages of detection [11].

Table 2-1 shows incidence and prevalence data for ovarian and endometrial cancers. According to the WHO[14], in 2004 there was a total of 24,000 DALYs[7] lost due to ovarian and endometrial cancer in Canada alone. Table 2-2 summarizes the overall 1- and 5-year survival rates for OVECA by stage at diagnosis.

The etiology of OVECA is not yet fully understood; however, they can be categorized by their histologic origins as epithelial, transitional, or squamous. Eighty percent of OVCAs are epithelial, with high-grade serous being the most problematic due to their usual diagnosis at late stages. EDCA presents with a somewhat mirrored histologic origin, with 80% of epithelial cancers being of the endometrioid type; Table 2-3 and Figure 2-3 provide more detailed information on the different types of OVEDCA and their prognosis.

Table 2-2 — Overall survival rates for patients with epithelial ovarian or endometrial cancer. [6],[49],[50]

	Epithelial Ovarian Cancer		**Endometrial Cancer**	
FIGO Stage	**1-Year Survival**	**5-Year Survival**	**1-Year Survival**	**5-Year Survival**
I	96–100%	83–90%	98-99%	91-93%
II	93–94%	65–71%	94-96%	70-77%
III	85–88%	33–47%	82-85%	45-50%
IV	72%	**19%**	45-49%	**17%**

The progression of the disease depends on the origin, and the grade of differentiation of the tumorous cells. Initial stages begin with confined tumorous cells, that depending on their differentiation will remain confined or will begin to spread to adjacent and/or distant regions. Figure 2-4 illustrates and correlates the metastasis of OVCA to the stages and prognosis.

[7] DALY: Disability-Adjusted Life Year (Years of Life Lost + Years Lost to Disability)—1 DALY equals to 1 lost year of healthy life

Table 2-3 — Review of epithelial cancers based on the 5-disease classification by Prat [49]–[51]

Pathologic class		% of Epithelial cancers		Median Age (years)	Molecular abnormalities	Prognosis
Serous	**OVCA**	75-80%	**G3** 95%	64	P53 /BRCA	Poor
			G1 <5%	43	BRAF, KRAS	Intermediate
	EDCA	10%		67	P53	Poor
Mucinous	**OVCA**	10%		45-50	KRAS, HER2	Favorable
	EDCA	1—9%		45-50	KRAS	Favorable
Endometrioid	**OVCA**	10%		40-45	ARID1A, PTEN	Favorable
	EDCA	80% (G1-G3)		40-45	PTEN, KRAS, ARID1A, PIK3CA, CTNNB1	Favorable
Clear Cell	**OVCA**	3.7—12.1%		55	HNF1b, ARID1A, PIK3CA, MET	Intermediate
	EDCA	1—4 %		67	P53	Poor

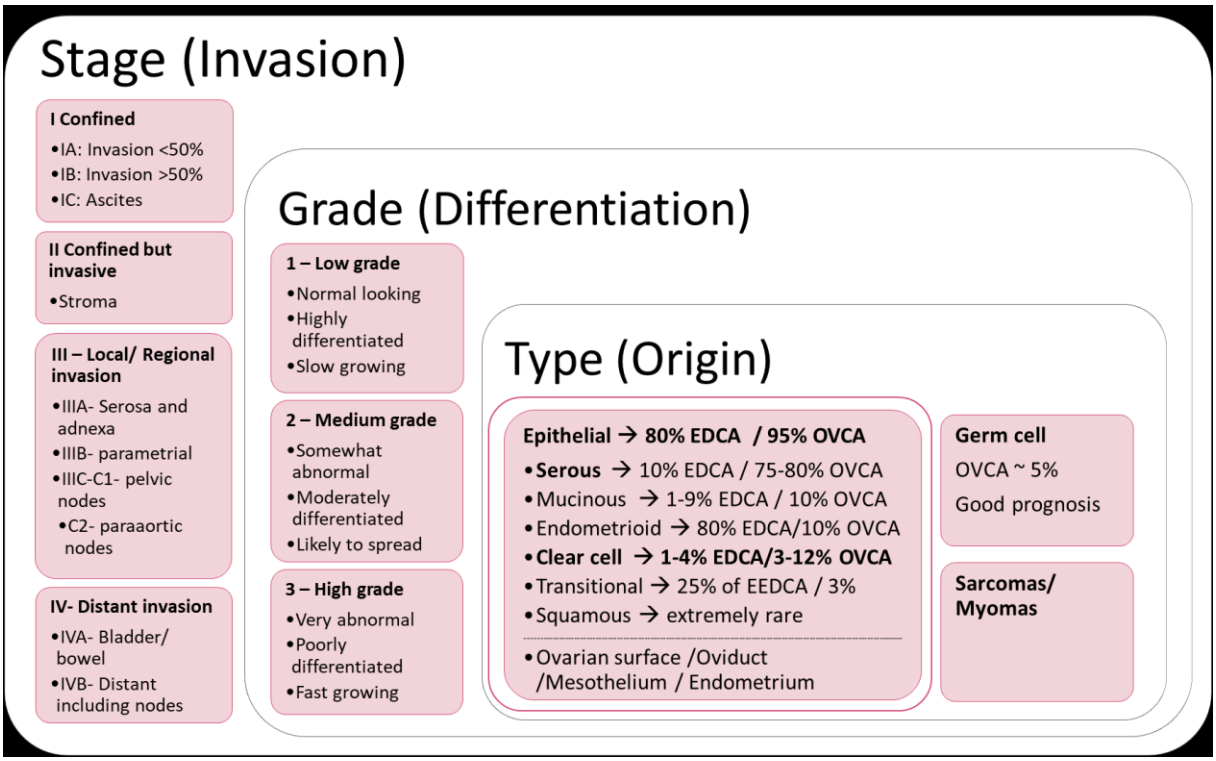

Figure 2-3 — Ovarian and endometrial cancers by type, grade, and stage. With information from [52]–[55]

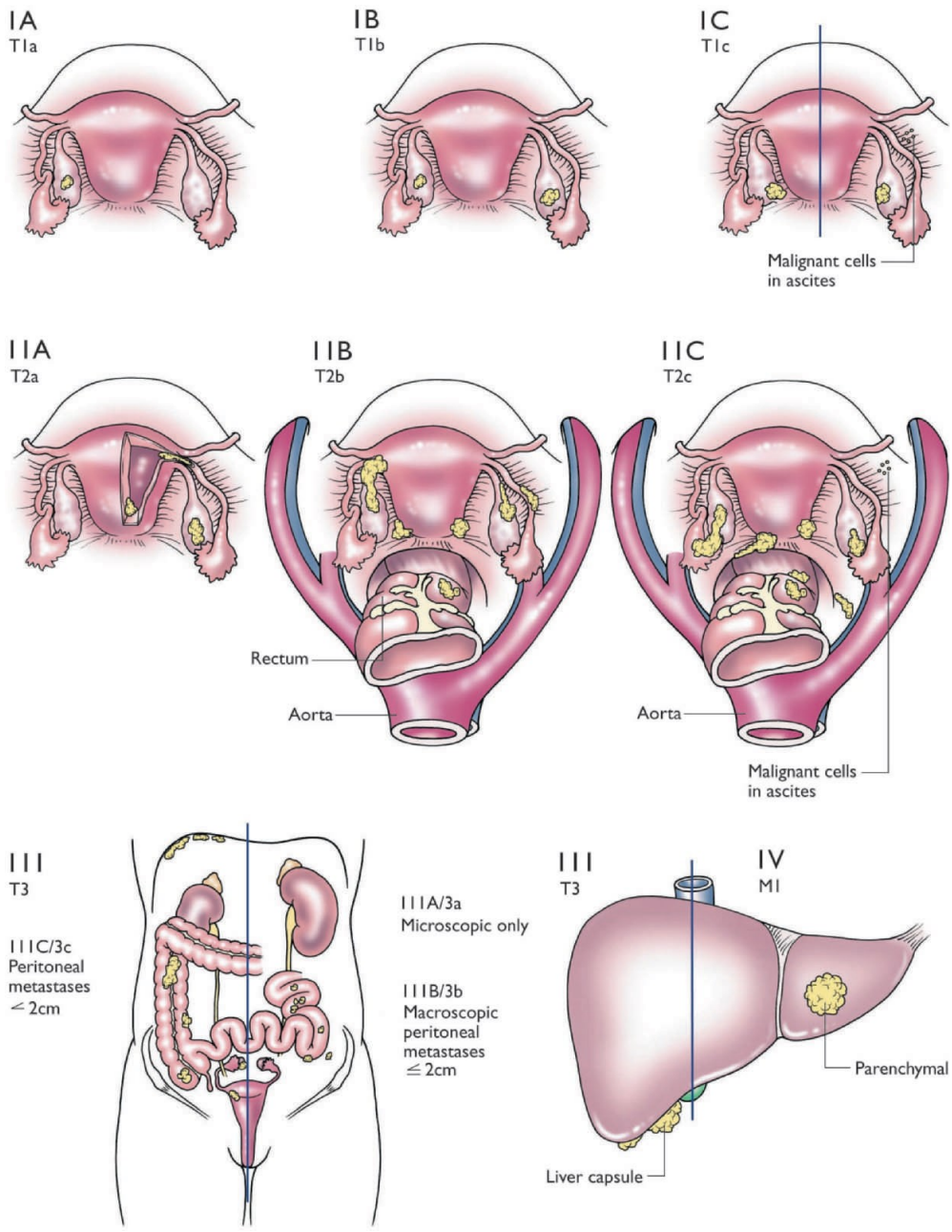

Figure 2-4 — Carcinoma of the ovary. Staging ovarian cancer: primary tumor and metastases (FIGO and TNM). With permission from [24]

2.2.2 DIAGNOSTIC AND THERAPEUTIC SOLUTIONS

OVCA and EDCA present without specific symptoms, which may include abnormal bleeding, vaginal discharge, lower abdominal cramps, abdominal pain or bloating, early satiety and/or urinary urgency or frequency (Table 2-4). These characteristics makes the disease hard to detect at an early stage. Differential diagnosis with benign gynecological conditions is determined using a series of tests and exams on a case -by -case basis.

These exams include a physical examination, routine laboratory exams, pelvic and chest imaging for metastasis, endocervical or endometrial cytology, as well as genetic testing before surgery, which remains the main therapeutic option.

Table 2-4 — OVECA symptom index and ACOG guidelines. Data from [56],[57]

OVARIAN CANCERS SYMPTOM INDEX	**ACOG[8] guidelines premenopausal women with mass suspicious for OVCA**	**ACOG guidelines postmenopausal women**
Development of, change in and/or persistence in:	**1 or more of:**	**1 or more of:**
Bloating	CA125>200U/mL	Elevated CA125
Pelvic or abdominal pain	Ascites	Ascites
Difficulty eating or feeling full quickly	Evidence of abdominal or distant metastasis	Nodular or fixed pelvic mass
Urinary symptoms of urgency or frequency	Family history of 1 or more first-degree relatives with ovarian or breast cancer	Evidence of abdominal or distant metastasis
ENDOMETRIAL CANCERS SYMPTOM INDEX (in addition to OVCA)		Family history of 1 or more first-degree relatives with ovarian or breast cancer
Abnormal uterine bleeding	Irregular menstrual bleeding, spotting, bleeding between periods	Any bleeding

The main treatment for OVCA and EDCA is surgery, including total hysterectomy with bilateral salpingo-oopherectomy and staging with pelvic and periaortic lymphadenectomy. Radiation therapy as a primary approach is only indicated for patients who cannot undergo

[8]American Congress of Obstetricians and Gynecology

surgery or present with advanced pelvic disease.[21],[24],[49],[58] Adjuvant or combination therapies are also available, including radiotherapy or chemotherapy as initial therapies; or a combination of either one with surgery as primary therapy.[24]

Despite advances in the treatment of ovarian cancer, to date there is no effective screening methodology for early detection relevant for the general population.[48]

2.2.2.1 APPROACHES FOR DETECTION AND SCREENING

Cancer antigen 125 — CA125 is a large membrane glycoprotein [21], recognized by the OC125-murine monoclonal antibody although it is found in greater concentrations in cancer cells, it is widely distributed in adult tissues [59], and higher levels can be found not only in OVCA and EDCA, but also in cancers that have spread to the peritoneum, like pancreatic, stomach, liver, or breast and lung cancers. It is used as a monitoring tool for at-risk or diagnosed patients. Only 50% of stage I OVCA and 75% to 90% of advanced cases present elevated levels of CA125[48]. Other tumoral markers can be found in Table 2-5.

Transvaginal ultrasound (TVUS) — Ultrasound imaging allows the observation of the ovaries and uterine cavity and the identification of changes in the structures and the possible presence of masses, as well as other abnormalities. However, a mass or any other abnormality must be observable and persistent to be considered for differential diagnosis without the risk of a false-positive.

A combined screening approach using CA125 and TVUS has proved to be more effective than either approach alone. [15],[49],[60]–[62]

Table 2-5 — Ovarian tumoral markers and their clinical significance [48],[63] [64]

Marker		Significance	Clinical levels	Tumor type
CA125	Serum Cancer Antigen 125	Prognostic, circulating correlates with stage and tumor burden	High levels indicate ovarian tumor	Epithelial tumors
HE4	Human Epididymis protein 4	Prognostic, circulating correlates with stage and tumor burden	Increases by ≥ 25% associate with relapse	
α-FP	Alpha fetoprotein	Diagnostic and prognostic; circulating and nonspecific (liver cancer)	Levels vary by age and sex	Germ cell tumors
β-hCG	beta-human chorionic gonadotropin	Diagnostic and prognostic; Only rules in the presence of a tumor, does not rule out presence of tumor	> 0ng/mL	

Endometrial biopsy — Endometrial biopsy is a cost-effective test that can be performed in the outpatient clinical setting. Samples of endometrium and fluids from the uterine cavity are collected and sent out for further cytology/histology-based analysis.

It is believed that the amount of endometrium removed from an endometrial biopsy reflects the adequacy of a sample for cytology- and/or histology-based diagnosis [65], however, diagnosis remains linked to the availability of tissue and the probability of collecting a representative sample. These limitations for tumor genetic analyses call for new methodologies[66]. One such methods is called liquid biopsy, which aims at identifying tumoral DNA in the form of cell-free circulating DNA (ctDNA) and circulating tumor cells (CTCs) typically in the bloodstream[67]–[69]. However, the same principles can be used to identify these genetic and protein markers in any biofluid sample[68],[70]–[74].

Maritschnegg et al [18] proved that tumor cells from ovarian neoplasms are shed into the uterine cavity, where they can be collected via lavage of the uterine cavity. However, the tools available for the collection of liquid samples from the uterine cavity are limited, often complicated to use, require specialized equipment and are painful and uncomfortable for the patients.

Currently available endometrial sampling devices (Table 2-6), have been so far designed for tissue-based cytology, where the retrieval of a strip of tissue is essential. Vacuum-based curettes like the Pipelle®, the Accurette® and the Explora® are based on the combination of cutting edges or ports and suction, either by an internal piston, a vacuum syringe or a vacuum pump. Brush-based devices, like the TAO Brush™ rely on abrasive force of nylon fibres to dislodge tissue from the uterine lining. These devices are shown in Figure 2-5.

Table 2-6 — Outpatient endometrial sampling devices — adapted from [75]

TYPE	MANUFACTURER	DIAMETER	DESCRIPTION
Vacuum-based			
Accurette®	Axcan, Plattsburg USA	4 mm	Flexible plastic curette with four cutting edges within a tube; aspiration with syringe
Explora ®	Cooper Surgical	3 mm	Flexible plastic curette with a large single tooth cutting edge
Gynoscan ®	Pedema AG	3 mm	Flexible curette consisting of two wings and a loop contained within a tube
Karman cannula ®	Rocket Medical	4-6 mm	Plastic cannula with two distal opposing ports
Pipelle ®	Cooper surgical	3.1 mm	Flexible cannula with a distal side port and an inner piston to generate suction
Tis-U-trap®	Cooper surgical	2-4 mm	Flexible plastic curette with a self contains tissue filter and electric suction pump
Z-sampler®	Zinnanti	3.1 mm	Flexible cannula with a distal side port, tapered tip and an inner piston for suction.
Brush-based			
TAO Brush ™	Cook Medical	3 mm	Flexible braided wire brush with a distal round tip.

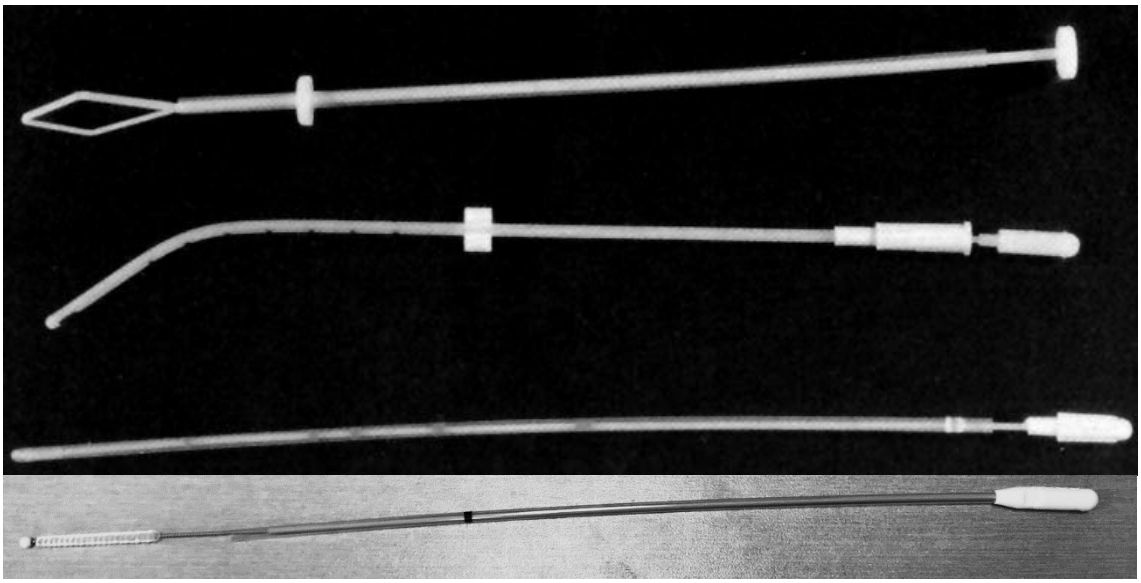

Figure 2-5 — Top to bottom: Accurette®, Explora®,Pipelle®[76] *and TAO Brush ™ endometrial sampling devices.*

3 BIOMECHANICAL BACKGROUND

Biological tissues are built hierarchically, and as composite materials, their mechanical properties are strongly related not only to those of their constituents, but also their geometric arrangement and organisational properties. The ECM proteins together with the functional cellular components are organized to provide specific mechanical properties, related to the organ's function, maintained by a self-stimulated cycle in which the forces acting on the organ as a unit affect the structure at the cellular level to maintain homeostasis and structural integrity.

It is known that pathologically induced mechanical alterations to biological tissues can lead to the onset of other pathologies. In the case of the female reproductive organs, these alterations can lead to multiple health issues in all stages of life, ranging from pelvic floor disorders (PFDs) to preterm birth, amongst others. However, the mechanical characterization of these tissues remains a challenge, mainly due to the variability and complexity of the structures; the lack of clear testing guidelines and protocols, and the superficial aspect of research available in the field to date [77]. For a long time, the bulk of female reproductive research was focused towards the understanding of the mechanics of pregnancy and the onset of labour. Yet a deeper and more complete understanding of the mechanical properties of the female reproductive organs that allows for women's reproductive and sexual health remains unmet.

Understanding the mechanical properties of these organs and tissues, and their relation to the onset of pathological states, can potentially lead to the identification and development of new prevention, detection and treatment strategies; as well as the development of tools for the evaluation of new technologies, and aid in the training of healthcare professionals.

In this chapter, we will discuss the mechanical considerations relevant to the design of an intrauterine sampling device and its testing and characterization.

3.1 MECHANICAL PROPERTIES OF LIVING TISSUES

Structural and material properties can be obtained by means of different *in vivo* and *ex vivo* testing. Ex vivo techniques include uniaxial and biaxial tensile and compressive tests, inflation, aspiration, puncture and indentation tests. *In vivo* methods include tensile, suction, ultrasound-based and inflation tests. When combined with histological and microscopy data, they can be used to guide the development of constitutive equations, then implemented into finite element and other numerical models. [78] or physical models for the testing and development of new technologies.

3.1.1 MECHANICAL CONSIDERATIONS OF SOFT TISSUE

Uterus — Uterine tissue has been tested *ex-vivo*. Conrad et al. first measured the passive stress relaxation of uterine muscle in pregnant and non-pregnant human tissue excised at the time of hysterectomy or caesarean section, they found uterine tissue from pregnant women to be more compliant and observed a lower stress relaxation rate than non-pregnant tissue (Figure 3-1) [79][80]. Pearsall and Roberts performed uniaxial tensile and compressive tests to explore the mechanics of human uteri obtained after normal vaginal hysterectomies. They discovered that the stress increases exponentially with strain and that the stiffness of the myometrium was lower under compression than in tension (Figure 3-2). Their findings revealed the anisotropy of the tissue, determined by the orientation of collagen and muscle fibres[81]. Kauer et al. performed aspiration tests and explored the behavior of uterine tissue excised from different physiological locations and found that the properties of uterine tissue were location-dependent[82]. Manoogian et al used uniaxial and biaxial testing methods on human and porcine uteri and determined the non-linearity of the stress-strain behaviour of the tissue. [83],[84].

Goldstuck et al. evaluated the uterine resistance to puncture (toughness) *in vitro* using freshly excised tissue and found puncture forces equivalent to 2-3 [N/mm^2] (20.7 - 28.4 N) of myometrial surface area.[85],[86] Turok et al. assessed the mean *ex-vivo* compressive force required to cause uterine perforation as 20 N (5.8 - 42.3 N). [87]

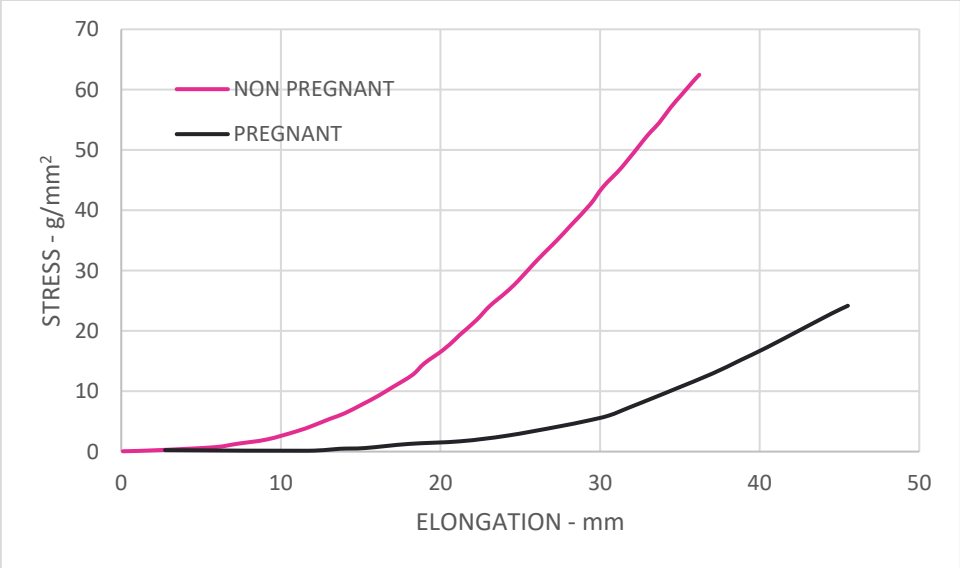

Figure 3-1 — Passive length-tension curves of human myometrium obtained from 3 -cm. long strips of pregnant and nonpregnant tissue. Adapted from [79]

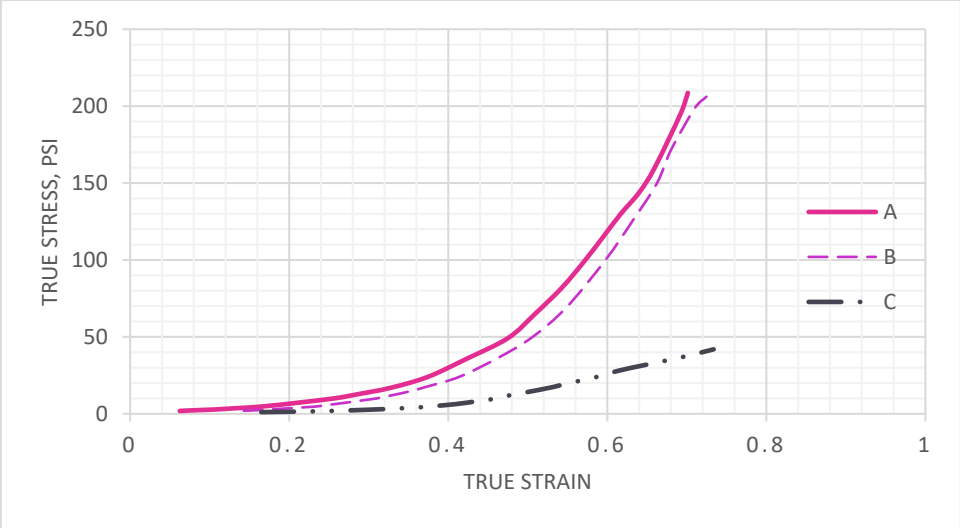

Figure 3-2 — Tensile and compression data for three specimens of myometrium taken from a single uterus. Curves A and B represent tensile data while curve C represents compressive data. Adapted from [81]

Cervix — Cervical tissue has been tested *ex vivo* under uniaxial tension and compression. *In vivo* testing included aspiration and indentation methods. Myers et al. performed ring uniaxial tension and compression tests on excised cervices from pregnant and non-pregnant women[39] and found a nonlinear stress-stress response; tissue was notably stiffer under tension than on compression. Cervical tissue from parous[9] women was found to be more compliant than that of nulliparous women. Myers et al. also observed a stiffer response on the external *os* when compared to that of the internal *os* [39]. When comparing results from *in vivo* and *ex vivo* specimens subjected to aspiration testing, Mazza et al. [88] found no significant difference in stiffness, creep, or rise time. In indentation tests, Yao et al. found that tissue had a time-dependent response and observed that age, parity, pregnancy and specimen location had an impact on the mechanical properties observed; non pregnant tissue showed larger shear moduli than pregnant tissue, and an increase in the number of vaginal deliveries correlated with a stiffer cervix[89]. As for the mechanical dilation of the cervix, Young and Craven studied the relationship between longitudinal force and dilation, and created a model to predict the amount of tissue damage for any given dilation[90], which can be in turn correlated with pain. In other studies, a correlation was established between the presenting surface area of the inserter tube and the force required for its insertion[85],[86],[91],[92], as well as the parity and gestational age, [92] Fisher et al introduced the concept of a cervical resistance index (CRI)[92]–[94]. Table 3-1 shows the insertion forces from several dilators and intrauterine device inserters. In another study, Goldstuck et al showed that when cervical resistance forces are greater than those withstood by the inserted devices, these show "bowing" or kinking[95].

[9] Parity refers to the number of births a woman has given to throughout her life.

Table 3-1 — Longitudinal forces required to insert an intrauterine device and to dilate the cervical canal. Adapted with permission from [86]

Study	Dilator (mm)	Mean force (N)
Anthony et al.[92]	Hegar 3	**2.45**
	Hegar 4	**3.43**
	Hegar 5	**8.33**
Nicolaides et al.[91]	Hegar 3	**1.3**
	Hegar 4	**1.4**
	Hegar 5	**3.4**
Goldstuck [85]	Copper-7® *3.07	**1.5**
	Nova T200® * 3.6	**2.13**
Notes: * Presenting diameter of intrauterine device inserter tube; Copper-7, GD Searle and Co (High Wycombe, UK). Nova T200, Bayer, (Wuppertal, Germany)		

Cervical dilation and pain — Pain in the inner female reproductive tract arises from distention, injury or inflammation, also called visceral nociception [10] [96]. Tingaker et al identified the presence of sensory corpuscles in the uterus and the cervix[97], identified as Pacini and Ruffini-like corpuscles. These corpuscles are known to react to distension and pressure (mechanoreceptors); they play a role as starting points of sensory pathways and convey proprioceptive information.

The insertion of a device through the cervical canal and into the uterine cavity produces mechanical stimulation via stretching of these pain receptors at the internal *os*, and both mechanical and chemical stimulation of pain receptors throughout the uterine body[98]. Young and Craven modeled the cervix as a thick cylinder of isotropic, homogeneous and incompressible hyper-elastic material under internal pressure and used this theoretical approximations to predict

[10] From latin *nocere* to harm or to hurt; refers to the sensory nervous system response to harmful or potentially harmful stimuli.

tissue damage for any given dilation and dilation rate required to minimize damage and compared their results to experimental data[90]. They found that if present, the friction coefficient would not exceed 0.05, and that irrespective of the longitudinal (axial) force applied for dilation, tissue damage, i.e. rupture, occurs at a critical extension ratio, dependent of dilation and dilation rate.

The response to pain at the cervical *os*, although subjective, is then correlated with the degree of stretching and deformation sensed by local corpuscles, and hence to the diameter and profile of the device inserted and the cervical resistance to its insertion (CRI).

Lower profiles (diameters), together with slower dilation rates will present with a significantly lower overall deformation, directly related to the longitudinal insertion force and the corresponding cervical radial force generated[90],[98], which can then be used for the definition of an “objective” pain scale for *in vitro* device performance evaluation purposes.

3.1.2 MECHANICAL CONSIDERATIONS OF BIOFLUIDS

As previously mentioned, the functional epithelium that lines the genital tract secretes fluids with different functions, in this section the mechanical characteristics of these fluids and their impact on the design and performance of intrauterine devices and procedures will be discussed.

Intrauterine fluid (IUF) — Due to its low availability (average volume < 1.5 mL) and the ethical and technical difficulties for sourcing[31], human IUF has not been fully characterized thus far[34]. However, Allen et al. have studied the rheological properties of estrous uterine fluid in mares, and have found this biofluid to be non-Newtonian, with a linear viscoelastic strain region between 5 and 20% strain (Figure 3-3) [30]; and an apparent instantaneous viscosity at low shear rates of about 1000cP[99].

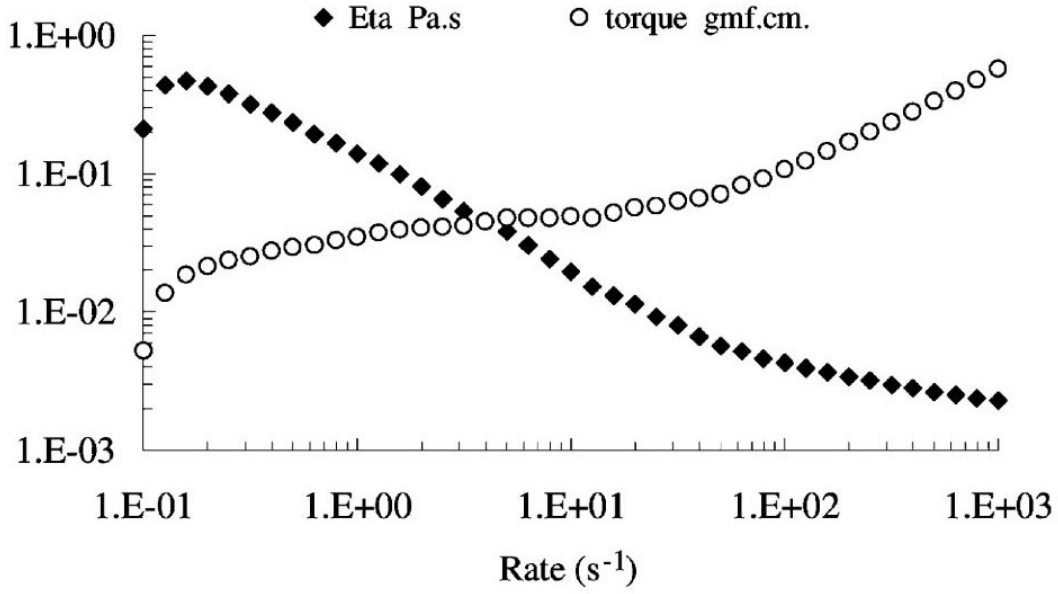

Figure 3-3 – Apparent viscosity of intrauterine fluid of estrous mares with increased rate of shear stress. Reproduced with permission from [30]

The composition and mechanical properties of IUF have an impact on the overall transportation of cells and molecules into and within the uterine cavity and are highly sensitive to hormonal influence. Roberts et al. studied the composition of IUF and found a variation in the protein content of 1-21 mg, with a lower protein concentration around the time of ovulation (mean 3.1 mg.), and higher just before the start of menstruation; for post-menopausal women, the protein content in IUF was between 8-14 mg[31]. It has also been established that a higher

content of protein increases the viscosity of fluids[100]. Clinically speaking, these impact natural and assisted reproduction; transport of cells and pathogens, including tumoral cells and cell-free DNA, potentially affecting metastasis and infection spreading, and consequentially, detection and therapeutic options.

Cervical mucus — This biofluid is more accessible than IUF due to its anatomical location and volume, and hence has been studied in more detail; however, the difficulties associated with sample acquisition render highly variable characterizations. Like IUF, cervical mucus is highly responsive to hormonal changes and presents with a high cycle-dependent variability. Its mechanical properties are modulated through the protein and water content. [25]–[28],[33],[101] It presents with apparent viscosities as low as 10-240 Poises at the time of ovulation, to allow for sperm penetration, and as high as 1000-1700 Poises by the end of the menstrual cycle[101],[102]. Its viscosity could impact the CRI.

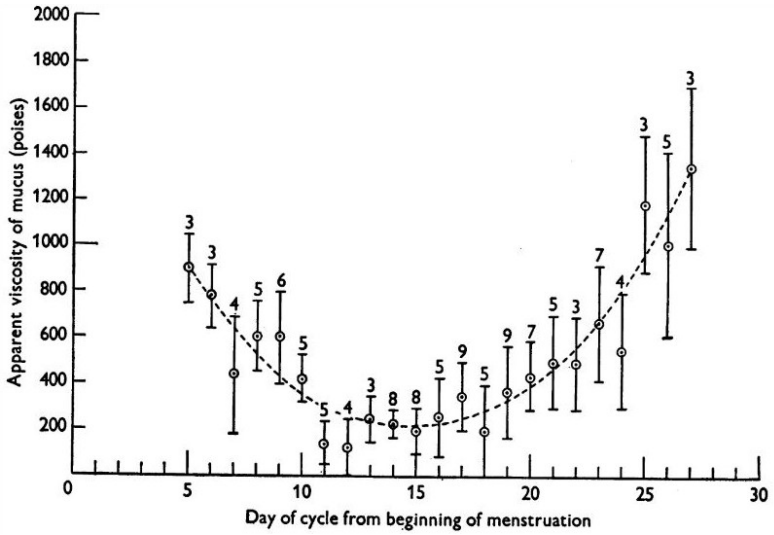

Figure 3-4 — Variation of viscosity of cervical mucus in healthy non-pregnant subjects (119 samples). The dotted line is drawn to emphasize the main feature of the graph. The number above each point indicates he number of samples averaged. Each vertical line indicates ± standard deviation of individual readings about the mean. With permission from [25]

3.2 BIOMEDICAL IMAGING SEGMENTATION AND MODEL GENERATION

The use of physical three-dimensional medical models has greatly increased as additive manufacturing technologies have evolved and become more available in the clinical and research setting. This section will address the process (Figure 3-5) for the successful generation of anatomically correct three-dimensional physical models, from data acquisition to application.

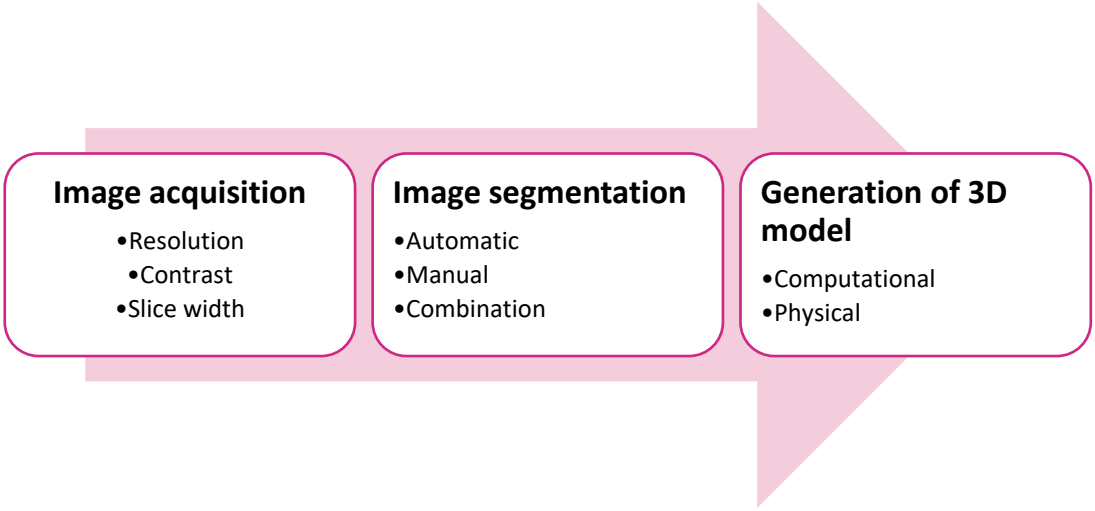

Figure 3-5 — Three-dimensional model generation from medical imaging.

3.2.1 IMAGING AND SEGMENTATION

Medical imaging techniques such as Magnetic Resonance (MR) and Computed Tomography (CT), provide bidimensional images of bodies at controlled distances and directions amongst each other and then use the relationship between these multiple contiguous projections to reconstruct the internal composition image of the original object (Figure 3-6), stored as spatial representations of energy intensity emitted from the object [103].

In the case of MR, images from the internal physical and chemical properties of the body are formed by measuring the nuclear magnetic resonance (MNR), and their quality depends on several factors, of which the contrast, the spatial encoding (resolution), the slice width and the signal to noise ratio (SNR) and contrast to noise ratio (CNR) are of particular importance for the three-dimensional reconstruction of medical images.

The image information is stored in voxels, or volume elements, which correspond to the smallest sampled element in a 2D image (pixel) and the slice thickness (Figure 3-6). Much like a regular scan or photograph resolution, the size of the voxel influences the final quality of the image.[104]

The process of tagging image pixels and/or voxels with meaningful labels such as anatomical structures and tissue types, is called segmentation [105], it also often represents the most time-consuming step of three-dimensional extraction.

In the case of complex anatomical structures, like the female pelvis, automated segmentations may not always be possible, and a semiautomated approach or user guided segmentation may be required[106],[107].

Segmentation of medical images is widely used for the generation of medical models[108]. In the case of the female pelvis, it has been previously used to assess new algorithms for the identification of well-defined structures [109], or the measurement of uterine fibroids [110]; the assessment of cervical changes during pregnancy [111]; preterm labor[112],[113] and childbirth simulation [107]; for surgical planning strategies [114],[115]; virtual reality training [116], or the generation of anatomically correct phantoms for *in vitro* testing of new technologies[117], amongst other applications.

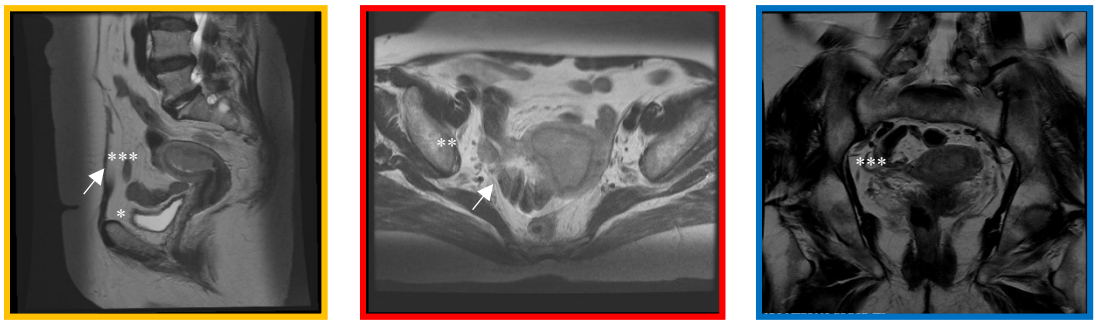

Figure 3-6 — Magnetic Resonance imaging of the female pelvis in different planes, left to right, sagittal (yellow), axial (red), oblique coronal (blue). The uterus (***), oviducts (**) and vagina (*) are observable in all three planes, with a clear radiopaque line delimitating the junctional zone (arrow). Extracted from research data.

MATERIAL SELECTION

Materials selection is key for the success of the model, it is important not only to replicate the geometrical features, but also the mechanical behaviour of the tissues involved. Polyvinyl alcohol (PVA) hydrogels have been widely used to represent the mechanical properties of different soft tissues, as their mechanical response can be fine-tuned by modifying the processing parameters such as the concentration, solvents, thermal cycles or thawing rate[118]–[126]. Silicone rubbers are also used because of their similar mechanical properties and added shelf-life, which makes them more suitable for multiple use models, however, they offer higher surface resistance and often must be used with a lubricant.

4 METHODS AND MATERIALS

This chapter presents the different methodologies used throughout this work, starting with the general design methodologies followed by the design results, in section 4.1.1. Details on the verification and validation testing methodologies used to establish safety and proof of concept follow: section 4.2 presents structural and integrity testing; *In vitro* performance tests are presented in section 4.3. Results for these sections will be discussed in Chapter 5.

4.1 DESIGN METHODOLOGIES: UTERINE COLLECTOR

Using a combination of the Pahl, Beitz and Pugh design models and a divergent-convergent model [127] described in Figure 4-1; a series of clinical and stakeholders' needs were identified and translated into design criteria (Table 4-1) and technical specifications, of which values and constraints are drawn from available information in the literature and from experimentation. Design for verification, validation and manufacturability was followed at all stages. Stakeholders identified include healthcare professionals, patients, payers, policy makers, and manufacturers amongst others.

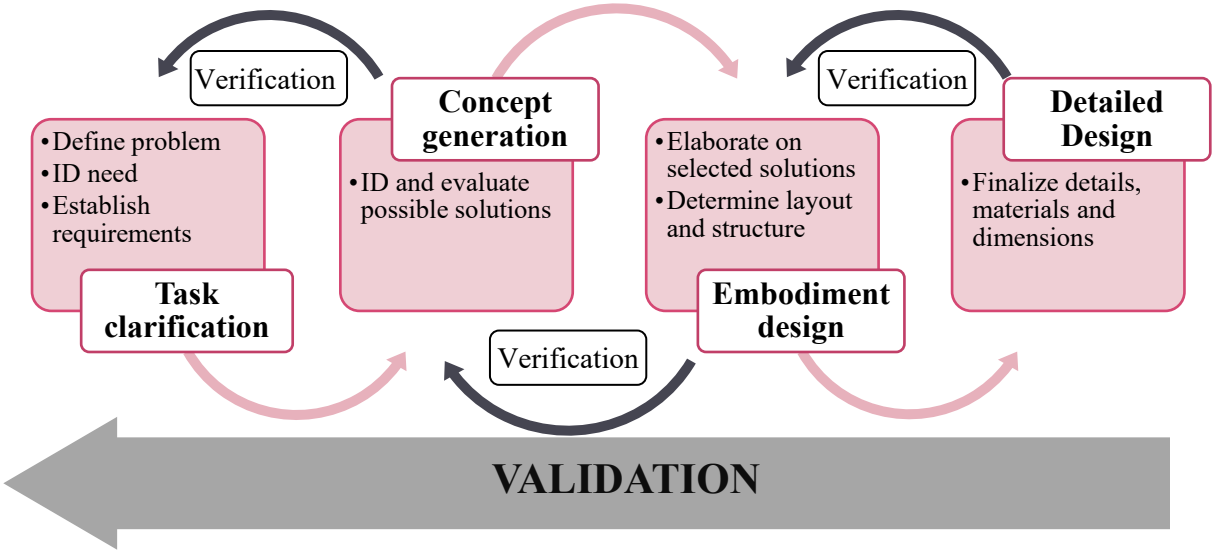

Figure 4-1 — Design process, including verification and validation cycles.

After a series of meetings with clinicians, the problem was identified and defined as the need for women's health professionals to obtain samples of "floating" DNA from the uterine tubes and fundus, in a quick, innocuous and painless manner, for ovarian and endometrial cancer screening in women 45 years of age or older.

Following this phase, a functional analysis was performed, the main functions were identified, and the functional and technical requirements were determined, which were then translated into technical specifications (Figure 4-2).

Table 4-1 — Design criteria and challenges

Ease of use	• Standard kit • Non disruptive • Requires fewer instruments / steps
Sample viability	• Adapts to anatomy • Reaches intended areas with ease • Protects sample • Vial design for sample preservation
Pain reduction	• Adapts to anatomy • Low profile (OD) • Does not disrupt endometrial lining

A series of conceptual designs were generated in collaboration with the clinical team at the MUHC, a group of undergraduate students and stakeholders, at which point, the converging designs were kept and further iterated to better fit the specifications. CAD modeling was used for the development of the conceptual designs, as well as the embodiment and final detailed designs.

Materials were chosen for biocompatibility, resistance to sterilization, as well as strength. Dimensions were computed to better fit both the anatomical average dimensions to account for anatomical variability, as well as mechanical properties, manufacturing limitations, and desired performance.

Prototypes were manufactured for verification and validation purposes. Feedback from clinicians and stakeholders was obtained and input back into the design process for the next iterations. Prototypes were manufactured and assembled by GSE Biomedical in Hermosillo, Mexico. GSE also collaborated in the analysis for manufacturability and provided us with great insight into the verification and validation processes, as well as the final documentation and transfer for manufacturing and validation.

Structural and performance testing for the assessment of safety and proof of concept were performed. Further testing and results are expected in a feasibility clinical study to begin in May 2020 at the Research Institute at McGill University Health Center (RI-MUHC).

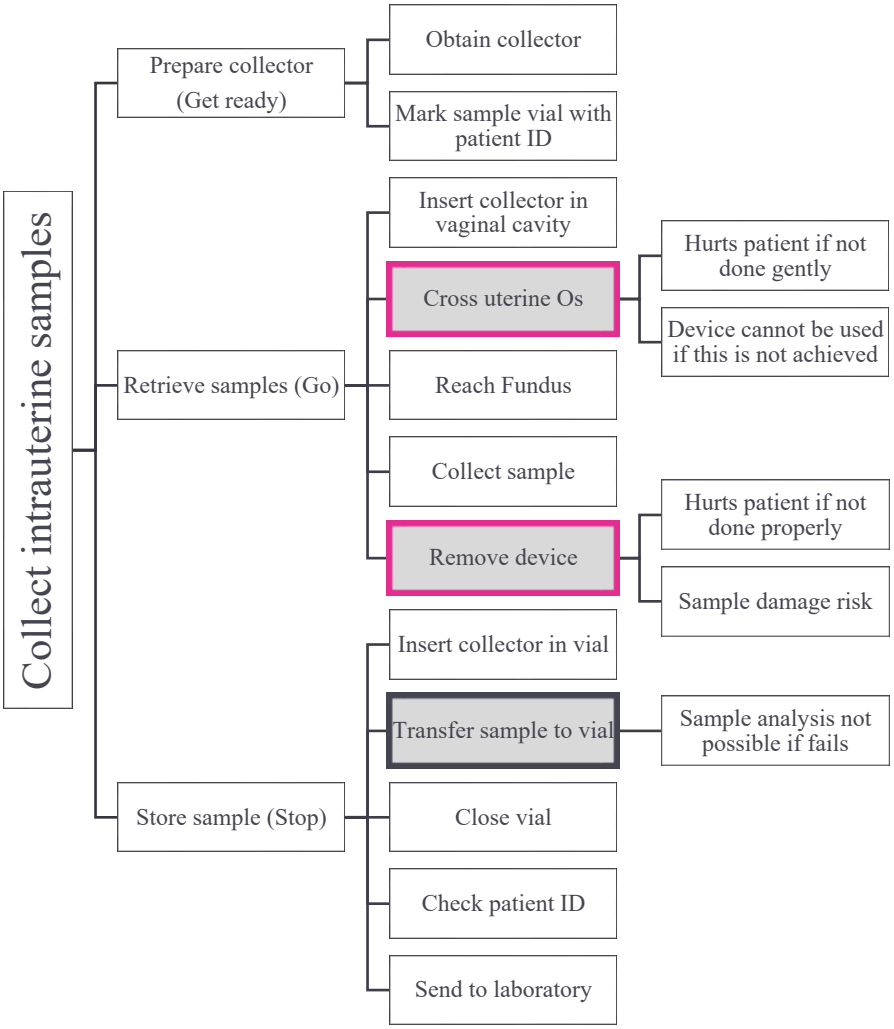

Figure 4-2 — FAST diagram for an intrauterine sample collector. Shaded entries denote critical steps in which failure can occur, directly related to the devices' operation (red entries), related or not related to the devices' operation (gray entries)

4.1.1 UTERINE LIQUID BIOPSY SAMPLER DESIGN

Four concepts were generated to comply with design criteria and specifications shown in Table 4-2. Two were selected for prototyping based on manufacturability, the only difference between them being the final configuration of the collection surface. These iterations are here on identified as UC-A01 or collector A (Figure 4-3) and UC-A02 or collector B. Figure 4-4 shows the differences between design.

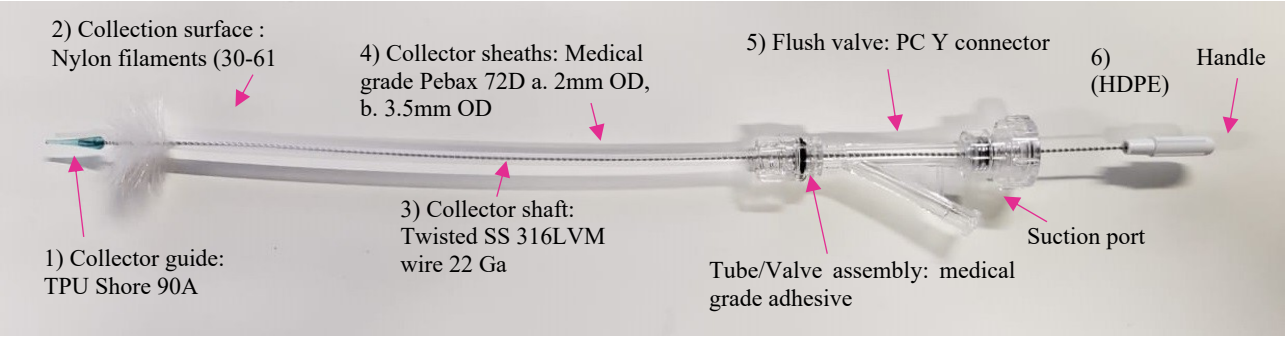

Figure 4-3— Uterine liquid biopsy collector (UC-A01), components and materials.

Table 4-2 — Design criteria for proposed solution for early detection of ovarian and endometrial cancers

Criteria	Specification
Sterilizable	EtO gas / Gamma rays
Ease of use	Simple / No need of specialized training
Pain reduction	<3.5 on a 0-10 scale
Sample quality	High sample content in low volume
Volume collection	~ 1 mL
DNA inert	Yes
Reusable	No
Affordable	Yes < C$20.00

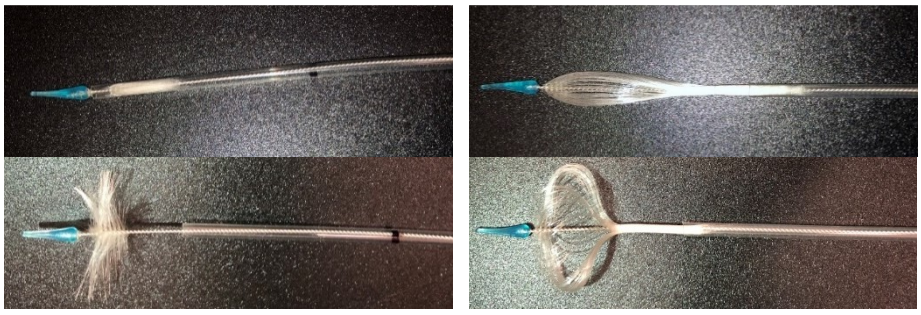

Figure 4-4 — Detail of uterine liquid biopsy collector surfaces in UC-A01 (left) and UC-A02 (right) before (top) and after (bottom) deployment.

Materials were chosen for biocompatibility, manufacturability and regulatory compliance, their mechanical properties are detailed in Table 4-3. All concepts comprise a tapered tip for a progressive cervical dilation (collector guide) (see section 3.1.1—*Cervical dilation and pain*); a soft, fibrous surface for cell recovery (collection surface); a suction/injection port and a sheath for sample protection. Suction is achieved by means of a standard syringe. These features provide added functionalities including: 1) progressive cervical dilation for pain reduction; 2) suction for added volume collection and 3) flushing / injection for therapeutic indications or aid in collection. Figure 4-3 shows the uterine liquid biopsy collector components and materials.

Table 4-3 — Mechanical properties of selected materials

	SS 316 LVM	**TPU**	**PEBAX**	**HDPE**
Modulus of elasticity	187.5 GPa	8.96 MPa	1.3 GPa	1.50 GPa
Compressive Yield Strength	170 MPa	—	—	23.0 MPa
Flexural Modulus	—	55.2 MPa	513 MPa	1.86 Gpa
Shore Hardness	—	94 A	66 D	50 – 76 D
UTS	1.3 – 2.2 GPa	62.1 Pa	56 MPa	43.0 MPa
Elongation at break	45%	400%	> 300%	3.2 %
Elongation at yield	—	—	18 %	3.0 %
Tensile stress at yield	190 MPa	—	26 MPa	43 MPa

Collector components, from distal to proximal, are: 1) a conical thermoplastic urethane (TPU) guiding tip (collector guide); 2) an arrangement of nylon microfilaments (collector surface); 3) a two-stranded braided stainless steel guidewire (collector shaft); 4a) a polyether block amide (Pebax®) inner sheath; 4b) a Pebax® protective sheath (collector sheath); 5) a polycarbonate (PC) hemostatic Y connector (flush valve); 6) a high density polyethylene (HDPE) handle (collector handle). The inner sheath in collector B also aids in the fixation and deployment of the collection filaments.

The collector shaft is cleaned with ethanol and dipped in a bonding agent (Loctite 4011, Henkel), before being embedded in the polymeric blocks. UC-B01 refers to the collector assembly (guide, shaft and handle) with no distinction as to the collection surface configuration. UC-B02 refers to the collector sheath/flush valve assembly. Detailed information on the components can be found in Table 4-4.

Table 4-4 — Materials selection and specifications

Component	Specification	Material	Rationale
Collector guide; *Os*-dilator	Ø: 1 – 3.5 mm ± 0.05 mm L: 15 mm ± 0.05 mm	**TPU Shore 90A**	Mechanical properties Processing Sterilization properties Regulatory Compliance
Collection surface filaments	Ø: 30 – 60 µm	**PA USP 8/0 Nylon**	DNA affinity inertness
Collector shaft: Braided wire guide	22 gauge Pitch: 1 mm ± 0.05 mm	**SS 316LVM**	Mechanical properties Corrosion resistance Component interaction Sterilization properties Regulatory Compliance
Collector sheath	*Inner sheath:* OD: 2 mm ± 0.05 mm WT: 0.13 mm ± .03 mm	**Pebax ® 72 D Medical tubing**	Low density Resistance to fatigue Dimension stability Versatile processing Sterilization properties Regulatory Compliance
	Outer sheath OD: 3.3 mm ± 0.07 mm WT: 0.13 mm ± .03 mm		
Flush valve: Y connector	Off the shelf Female Luer-Lock port 0 — 9 Fr. valve	**Medical grade PC, Silicone**	Component compatibility Sterilization properties Regulatory Compliance
Collector handle	Ø: 6.35 mm ± 0.55 mm L: 25mm ± 0.05 mm	**HDPE**	Manufacturability Sterilization properties Regulatory Compliance
Adhesive	UV Curable	**Medical Grade**	Sterilization properties Regulatory Compliance

Ø: diameter; L: length; OD: Outer diameter; WT: wall thickness; Fr. French

4.2 STRUCTURAL AND INTEGRITY TESTING

The purpose of this testing protocol is to define the rationale, test methodologies, test levels and pass/fail criteria for a critical component dislodgement validation using tensile tests, and to determine the strength and integrity characteristics of the critical and non-critical components. Table 4-5 summarizes the structural integrity tests, as well as their rationale.

Two design iterations were tested: UC-A01 (collector A) and UC-A02 (collector B). UC-B01 refers to the collector assembly (guide, shaft and handle) with no distinction as to the collection surface configuration. UC-B02 refers to the protective sheath/flush valve assembly.

Table 4-5 — Structural strength and integrity test summary

Test	Test Article	Rationale
Collector guide dislodgement force	UC-B01 — Collector Assembly TAO Brush™	CC – risk assessment device failure
Collector handle dislodgement force	UC-B01 — Collector Assembly TAO Brush™	NCC – integrity
Sheath dislodgement force	UC-B02 — Collector Assembly	NCC – integrity
Fibre dislodgement test	UC-A01 — Collector A UC-A02 — Collector B	CC – risk assessment device failure
Compressive strength test	UC-A01 — Collector A UC-A02 — Collector B TAO Brush™	Risk assessment – uterine perforation

*CC – critical component, NCC – non-critical component

4.2.1 TENSILE TESTING FOR MAXIMAL ADHESION STRENGTH (PULL-OUT FORCE)

THEORETICAL CONSIDERATIONS

A pull-out test is a simple way of measuring adhesion between two surfaces. The pull-out force increases when the contact area between both surfaces increases. The debonding fracture propagates through the interface starting at the embedded end. Thus, the pull-out force is directly related to the work of breaking the interfacial bond and the work of stretching the material [128] and the force of adhesion of the two surfaces.

In a rubber-metal interface, if the metallic rod is considered inextensible, and the elastic properties of the rubber are known, the fracture work per unit area of interface can be calculated [129]. For propagation of debonding along a rod by a distance *d,* work of detachment is given by

$$dW_1 = 2\pi r G_a d \quad (1)$$

where r is the radius of the rod and *Ga* the energy required to fracture a unit area of the material interface (rubber-rod). Work of deformation conveyed to the freshly detached portion of rubber surface is given by

$$dW_2 = (F^2 / 2AE)\, d \quad (2)$$

where *F* is the pull-out force, *A* is the cross-sectional area of the rubber block and *E* is the tensile modulus of the block material, assumed to be linear elastic. The work provided to the system by the additional extension of the block is given by

$$dW = Fe\, d = (F^2 / AE)\, d \quad (3)$$

where *e* is the elongation of the detached portion of rubber material under the pull-out force *F*.

Conservation of energy $dW = dW_1 + dW_2$ (4)

thus from (1), (2) and (3) in (4)

$$F^2 = 4\,\pi r A E G_a \quad (5)$$

Maximum force before component dislodgement was assessed by uniaxial tension on an Instron Electropuls E1000 (Instron Co.) mechanical tester with a ±2 kN dynamic load cell (Dynacell 2527-129, Instron Co.). Samples were mounted for a 0-degree test, as shown in Figure 4-6 and Figure 4-7; and held in place with MARK-10 grips and clamps (MARK-10 Co.). All tension tests were performed under dry conditions at room temperature with a preload value of 1 N, at 1 N/min and a displacement of 20 mm/min.

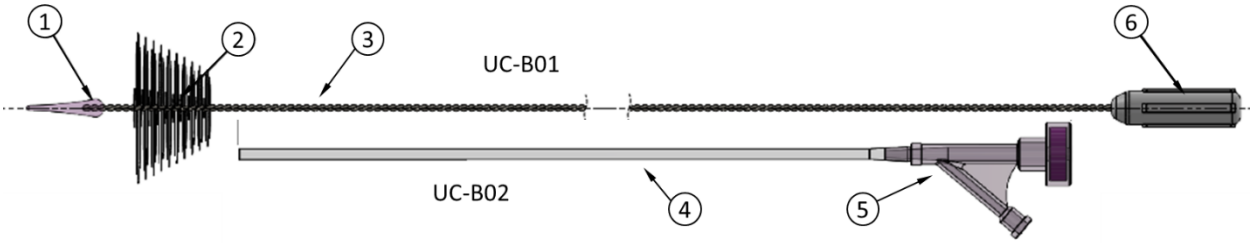

Figure 4-5 — Uterine liquid biopsy collector A, and subassemblies UC-B01 and UC-B02: 1) collector guide; 2) Collection surface; 3) Protection sheath; 4) Flush Y valve connector; 5) Collector shaft; 6) Collector Handle

Prepared specimens (subassembly UC-B01 Collector shaft and guide assembly) (Figure 4-5, top) were tested for maximal force needed for collector guide and collector handle dislodgement and/or yield. The test setup is shown in Figure 4-6.

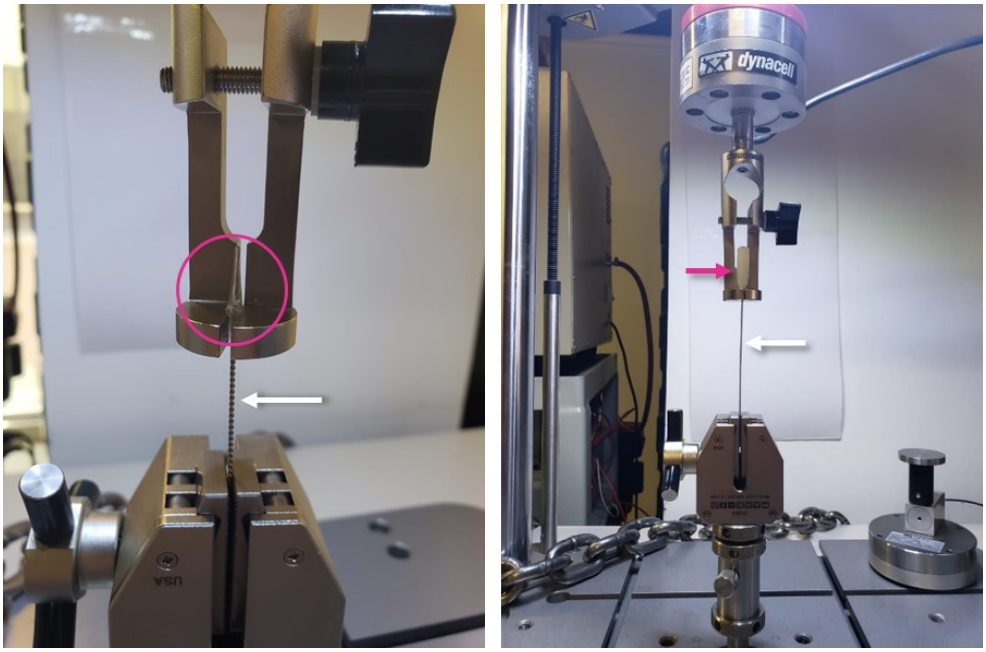

Figure 4-6 — Collector guide dislodgement test setup, Instron Electropuls e1000 (Instron Corp.). UC-B01 – Collector Guide (red circle), Collector Shaft (white arrow), Collector handle (red arrow)

Subassembly UC-B02 (protective sheath and flush valve assembly) (Figure 4-5, bottom) was tested for maximal force required for sheath dislodgement and/or yield. Test setup is shown in Figure 4-7. Test end conditions were determined as sheath yield or dislodgment from the valve port.

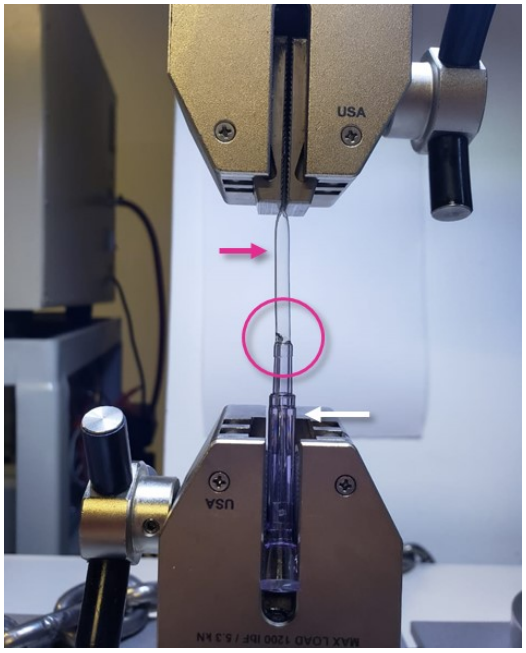

Figure 4-7 — Sheath Dislodgement Test Setup, Instron Electropuls e1000. UC-B02: Collector Sheath (red arrow), Collector Valve (white arrow), adhesion interface (red circle).

The samples were then loaded to failure at a displacement rate of 20mm/min. Maximum pull-out force and displacement were defined by the peak force and maximum displacement withstood by the samples prior to failure. Test end conditions were determined as collector guide/handle yield or dislodgement from the collector shaft and collector sheath yield or dislodgement from collector valve. Results for the collector guide, the collector handle, and the collector sheath are presented in sections 5.1.1.1, 5.1.1.2, and 5.1.1.3 respectively.

4.2.2 QUALITATIVE ASSESSMENT OF FIBRE DISLODGEMENT UNDER SIMULATED USE CONDITIONS AND PROBABILITY OF FAILURE

Given the diameter of the fibres used, a pullout test was not possible, and was replaced by a probabilistic approach for the observation of dislodged fibres under a worst-case scenario setting, defined as repeat use in a highly viscous environment.

THEORETICAL CONSIDERATIONS

The risk of failure can be assessed using probabilistic risk analysis (PRA) techniques, which quantify risk metrics, in this case the probability of fibre dislodgement under extreme conditions. Using a relative frequency approach, the probability of event A ***P(A)*** to happen can be calculated by

$$P(A) = \frac{N(A)}{n} \tag{6}$$

where *N(A)* refers to the frequency with which the event of interest ***A*** occurs, and ***n*** the number of experiments performed. Thus, an initially qualitative/binary analysis (i.e. pass/fail) can be associated to a quantitative assessment, in this case the probability of failure.

EXPERIMENTAL DETAILS

A pass/fail experiment was setup to evaluate the presence or absence of dislodged fibres from the collection surface into a solution simulating an extremely viscous intrauterine fluid (IUF)[25],[30], and the unlikely event of multiple uses.

Uterine collector design UC-A01 was used to assess the dislodgement of fibres under simulated conditions. The collectors were inserted in a 1.38-wt % gelatine solution at 4 °C and manually rotated 5 full counter-clockwise turns, by smoothly rotating the handle of the device between two fingers, and then pulled-out. After the rotation cycle was completed, the test articles (Figure 4-5) were removed, and the gelatine solution explored to evaluate the presence or absence of dislodged fibres.

A test is considered to fail if any fibres can be observed in the gelatine solution after cycling is completed. This was repeated a total of 30 times per specimen. Cycling was chosen to follow current practice, where an endometrial biopsy device is inserted into the uterine cavity and rotated clockwise or counter-clockwise 3 to 5 full rotations and then discarded after the sample is transferred into a vial.

The overweighed probability of a device being used multiple times was established as 0.1 (event A), and a combined probability of multiple uses (event A) and fibre dislodgement (event B) was calculated. Results are presented in section 5.1.2.

4.2.3 COMPRESSIVE STRENGTH FOR EVALUATION OF RISK OF UTERINE PERFORATION

THEORETICAL CONSIDERATIONS

Load-bearing structures that support tensile loads but are flexible in bending are categorized as rope or rope-like structures. These structures consist of redundant parallel load-bearing elements, operating as a whole; and can be analyzed as slender columns.

Columns fail by buckling or kinking when their critical load **F** is reached:

$$F = \frac{\pi^2 E \cdot I}{(kL)^2} \left[\frac{Pa \cdot m^4}{m^2}\right]$$

(N) *(7)*

where *k* represents a factor accounting for end conditions (effective length factor), *E* the material properties (modulus of elasticity), and *I* and *L* the geometric properties (second moment of area and the length of the column respectively).

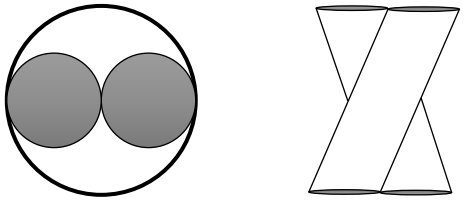

Figure 4-8 — Cross section (left), and side view (right) of a helical twisted wire assembly of two wires.

The resistance to bending of a helical structure such as a twisted wire (Figure 4-8) ; is given by the second moment of area, which for a solid circular cross section with radius *r* about its center line is:

$$I_c = \frac{\pi \cdot r^4}{4}$$

(m^4) *(8)*

If bending occurs about an axis that is offset from its own center line by a distance *d*, the second moment of area about axis I_i is:

$$I_i = I_C + Ad_i^2$$

(m^4) *(9)*

For a bundle of fibres assembled in such a way that there is no relative movement between each other, the superposition principle applies, and the second moment of area is equivalent to the sum of the individual I_i of the fibres about the center line of the bundle, or that of a circular bar of the same overall radius.[130]

$$F = \frac{\pi^2 E \cdot I}{(kL)^2} = \frac{E}{(kL)^2}\left(\frac{5}{2}\pi^3 r^4\right)$$

(N) *(10)*

Knowing a material's resistance to puncture, and comparing it to the column's critical load, one can determine if a column of a determined composition would buckle or perforate a block of material when a load F is applied. Figure 4-9 shows different end conditions accounted for by factor *k*.

Case:	**1**	**2**	**3**	**4**
Buckled shape of column	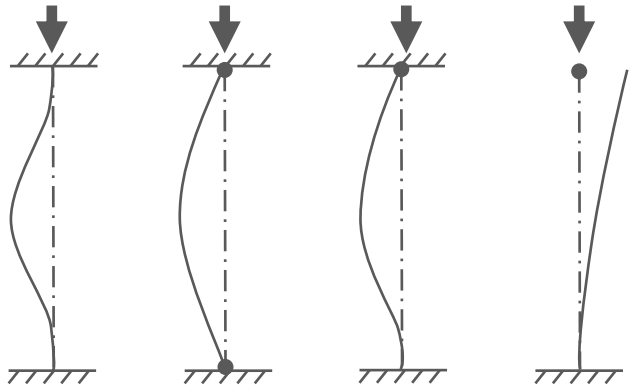			
End condition	Fixed ends	Pinned ends	Pinned end to fixed end	Free end to fixed end
Theoretical k value	0.5	1.0	0.7	2.0
Recommended design k	0.6	1.0	0.8	2.1

Figure 4-9 — Effective length factors. Theoretical values and recommended values when ideal conditions are approximated. Fixed ends allow for guided movement; pinned ends allow rotation about one or more axes.

Experimental Details

Theoretical resistance to bending was calculated for uterine collectors UC-A01 and UC-A02 in different scenarios and compared to typical intrauterine device insertion (Table 3-1) and uterine perforation forces obtained from the literature [85]–[87],[131] to obtain a safety factor and risk assessment for uterine puncture or device bending before insertion. Relevant material properties are presented in Table 4-3, relevant dimensions are found in Table 4-4. Devices should withstand insertion forces, and buckle before reaching the critical load associated with uterine tissue puncture, a complication of intrauterine procedures.

Clinical scenarios considered, summarized in Table 4-6, represent different column buckling cases, encountered at different stages of sample collection. The initial approach of the device on the external cervical *os*, right before insertion, when the collector guide is in contact with the tissue, and the handle is held by a health professional, can be represented by cases 2 or 3; Once the collector guide has been introduced into the cervical canal, past the external *os*, both ends of the collector are fixed (case 1). In the event the collector guide is placed within the cervical canal or uterine cavity, and the handle is released, a free to pinned end condition is present (case 4). Results are presented in section 5.1.2

Table 4-6 — Case conditions and effective length factors for buckling analysis

Case	Description	Clinical scenario	Theoretical k value	Recomm. k value
1	Both ends fixed	Guide within the cervical canal (fixed), handle held tightly (fixed).	0.5	0.6
2	Both ends pinned	Guide in contact with external cervical *os* (pinned), handle held loosely (pinned).	1	1
3	Pinned to fixed	Guide within the cervical canal (fixed), handle held loosely (pinned).	0.70	0.8
4	Free to fixed	Guide within the cervical canal/uterine cavity (fixed), handle not held (free).	2	2.1

4.3 IN VITRO PERFORMANCE

The purpose of this testing protocol is to define the rationale, test methodologies, test levels, and pass/fail criteria to characterize the intended use performance of the device. Section 4.3.1 describes the methods for sample collection and transfer; section 4.3.2 correlates the biomechanics of cervical dilation to pain; section 4.3.3 describes the assessment of ease of use and the generation of an anatomically correct uterine model.

Table 4-7 — Summary of in-vitro performance test protocols and rationale

Test	Test Article	Rationale
Volume collection test	UC-A01— Collector Assembly	Non-inferiority
	UC-A02 — Collector Assembly	
	TAO Brush	
Pain scale relation determination	UC-A01 — Collector Assembly	Patient discomfort
	UC-A02 — Collector Assembly	
	TAO Brush	
Ease of use under simulated conditions	UC-A01 — Collector Assembly	Overall performance Physician experience
	UC-A02 — Collector Assembly	
	TAO Brush	

4.3.1 VOLUME COLLECTION AND TRANSFER

THEORETICAL CONSIDERATIONS

The collection of volume from suspension can be estimated by a simple weight mass experiment.

From the equation of density, where $\boldsymbol{m}$ is the mass and $\boldsymbol{V}$ the volume,

$$\rho = \frac{m}{V} \qquad (\mathrm{kg/m^3})\ (11)$$

Thus, the density for a solution is the sum of mass concentrations of the components of the solution and is determined by,

$$\rho = \sum_i \varrho_i \qquad (12)$$

Where $\boldsymbol{\varrho_i}$ refers to the individual densities of the different components, and is expressed as a function of $\boldsymbol{\varrho_i}$ and their volume participation to the solution,

$$\rho = \sum_i \rho_i \left(\frac{Vi}{V}\right) = \sum_i \rho_i \varphi_i \qquad (13)$$

and the relationship between density and viscosity

$$\mu = \nu\rho \qquad (\mathrm{Pa{\cdot}s})\ (14)$$

where ν refers to the kinematic viscosity, and μ is the dynamic or absolute viscosity, and its dependence on changes in temperature [132] [133][134] expressed by

$$\mu(T) = Ae^{U/RT} \qquad (15)$$

where A is a constant representing the entropic factor, U[11] is the activation energy for shear flow, R is the gas constant and T the absolute temperature.

[11] Litovitz assumes the activation energy "E" as $E = {}^{a}/_{T^2}$ where $\boldsymbol{a}$ is the activation energy constant dependent on the specific properties and concentrations of the liquid.

Volume collection and solution concentration and resultant solution density and viscosities can be estimated. However, a quantitative assessment of concentration of a solute of interest in a solution can be obtained by spectrophotometry using the Beer Lambert Law.

When a beam of light of intensity I_0 crosses a solution of known length b, containing a light-absorbing substance, the intensity of the transmitted light decreases with the increase in concentration of the absorbing substance, hence the transmittance T is defined by, $T = {}^{I}/_{I_0}$.

The light absorbed by the substance is then represented by

$$A = -log(T) = \varepsilon_\lambda M b \qquad (16)$$

This principle can be used to calculate the concentration of a solution if its extinction coefficient is known. By measuring the absorbance (16) of a known concentration M of a solution, the wavelength dependent extinction coefficient $\mathcal{E}_\lambda$ can be determined and thus, the concentration of specific samples computed.

EXPERIMENTAL DETAILS

Volume collection was initially assessed by a mass to volume correlation and verification by comparing the known density and the calculated density. Samples collected were then analyzed by spectrophotometry to assess sample concentration.

SAMPLE PREPARATION

Collection was performed using both test articles, collectors UC-A01 and UC-A02; and a control, the TAO brush™. Figure 8-1 shows a flowchart of the collection process. Intrauterine fluid (IUF) was represented by 99% glycerin at 20 °C due to its similarity with the biofluids characteristics[29],[30],[135].

All devices and instruments were weighed before and after each step using an analytical balance (Quintix64-1S, ±0.1mg, Sartorius AG). A cold bath was prepared using a chilling plate (Ecotherm, Torrey Pines Scientific Incorporated) and a 350mL beaker filled with 300 mL of distilled water, to maintain a constant temperature of 20 °C ± 2 °C (JUI 14997, ±1°C, Fisherbrand™). A graduated cylinder (Class A, ±0.9 mL) with 10 mL of 99% glycerin dyed blue (FD&C Blue No.1), was weighed (Symmetry EC2000, ±0.05 g, Cole – Parmer®), and placed in the cold bath. Known density (ρ) and viscosity (μ) for 99% glycerin at 20°C ± 2 °C, are

1.26 g/cm^3 and 1150 centipoise (cP) respectively[136][137]. Figure 4-10 shows the experimental setup. Individual vials containing 5 mL of preserving solution were prepared and measured (mass and volume).

Ten measurements were taken with each test article. Collection was performed by inserting the test article at a 0-degree angle (vertical) into the graduated cylinder, immediately followed by 5 full cycles of counter-clockwise rotation by smoothly rotating the handle of each device between two fingers; after which the device was removed, and the sample transferred to a vial containing 5mL of methanol-based preservation solution (TP) (Preservcyt®, ThinPrep Pap Test, Hologic, Inc. Marlborough, MA) , after which aliquots of each sample were transferred to a 96-well microplate, as shown in Figure 4-10 (right), and analyzed in a TECAN SPARK M10 spectrophotometer for a quantitative measurement of the sample transferred to the preservation vial. A series of dilutions (dyed glycerine/TP) were prepared for spectrophotometer calibration.

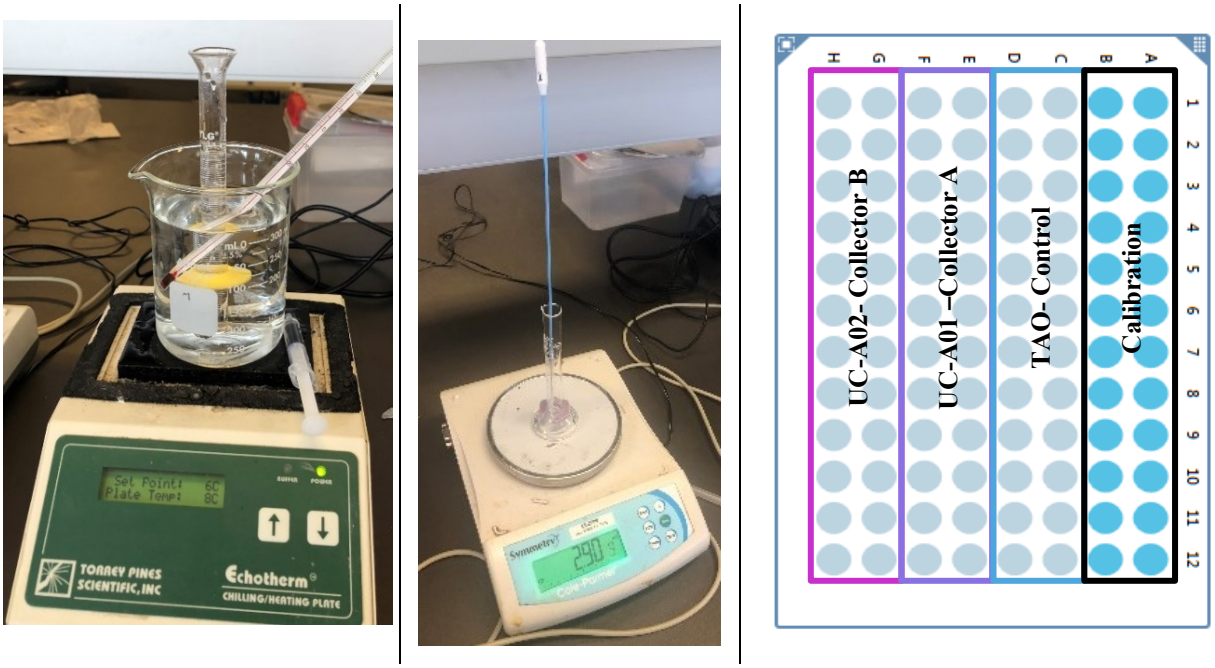

Figure 4-10 — Sample collection experimental set-up left to right: Cold bath; sample weighing after collection (control); Sample arrangement for spectrophotometry analysis and concentration determination

4.3.2 PAIN ASSESMENT: A QUANTITATIVE APPROACH

THEORETICAL CONSIDERATIONS

The Young and Cravens model for cervical dilation and tissue damage [90] was adapted to our devices' geometry and that of a commercially available device (TAO brush™, Cook Medical LLC, IN), and combined with literature-reported data on required forces for intrauterine device insertion, to obtain the theoretical radial force transferred to the cervical tissue, thus creating a quantitative approach to tissue damage and pain, which allows for the comparison of different devices with different geometries:

$$\boldsymbol{W = P\,cot(\alpha + \varphi)} \tag{17}$$

where $\boldsymbol{W}$ represents the radial force on the cervix; $\boldsymbol{P}$ the longitudinal force applied to the dilator and $\boldsymbol{\alpha}$ and $\boldsymbol{\varphi}$ the dilator taper angle and friction angle respectively[90]

EXPERIMENTAL DETAILS

Radial force transmitted to the cervical tissue was computed for a tapered collector guide profile, with a 3.5 mm diameter ($Ø_{min}$: 1 mm, α=4.76°) and compared to that of the TAO brush with a ball-point tip with a 3mm diameter (1:1, α = 60°). Longitudinal force $\boldsymbol{P}$, required for insertion, was taken from the literature, based on maximum insertion force reported for the device diameter as 2.5 N (Table 3-1); friction coefficient was assumed to be zero, due to the presence of lubricating fluids in the cervical canal.

The generated quantitative pain scale is to be compared and validated against patient perceived pain results from the clinical trial phase.

4.3.3 EASE OF USE UNDER SIMULATED CONDITIONS

This section refers to the generation of a thee-dimensional reconstruction of the uterine cavity (section 4.3.3.1) and the evaluation of ease of use of the device (section 4.3.3.2)

4.3.3.1 THREE-DIMENSIONAL RECONSTRUCTION OF THE UTERINE CAVITY

Anonymized magnetic resonance (MR) images of the female pelvic organs were obtained from the DOVEEgene trial (A08-M79-13B, NCT02288676) at the RI-MUHC.

Sagittal and axial T2[12] weighted FRSFE[13] MR images of the female pelvis were loaded into the segmentation freeware ITKSnap (ITKSnap 3.6.0)[106] and 3D Slicer (slicer 4.10.1) [138],[139], and the contrast was adjusted to highlight the anatomical structures of interest. The uterus, uterine cavity and vagina, as well as reference anatomic landmarks such as the bladder and iliac arteries, were identified using different semi-automated segmentation tools available in ITKSnap and 3D Slicer, followed by user inspection and correction, due to the complexity of the female pelvic anatomy and the radio-homogeneity of the different structures [109].

Once fully segmented, three-dimensional solids of the uterus and uterine cavity were generated, a series of smoothing filters were applied to fill in the gaps between slices and lower the stepwise appearance obtained from the segmentation alone. (Figure 4-11)

[12] T2 is a signal contrast protocol used in MR, obtained with long repetition and echo times.

[13] Fast Recovery Fast Spin Echo, or FRFSE, is a pulse sequence used in MR, provides high signal intensity of fluids and better contrast between tissues.

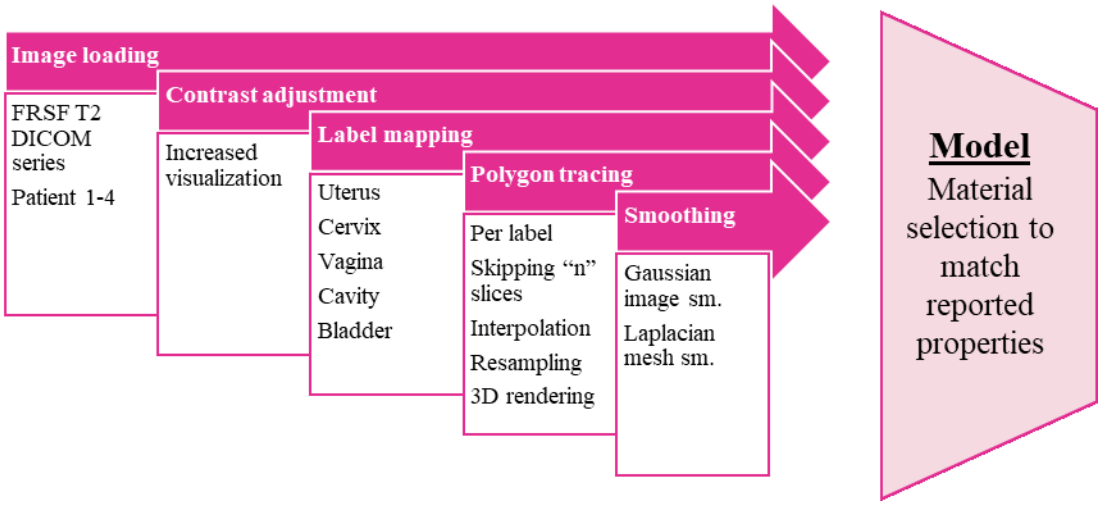

Figure 4-11 — Medical image segmentation workflow for three-dimensional model reconstruction.

Moulds of the uterine cavity and uterus were designed using Autodesk Fusion and 3D printed for the creation of a water-soluble isomalt-based negative of the uterine cavity, then used to cast a block representative of the myometrium and surrounding tissues on silicone rubber (ECOFLEX 00-10, Smooth-on Inc., PA). This model was then used to assess the anatomical compatibility of the uterine collector, as well as its ease of use, as a function of the steps required to successfully collect a sample.

4.3.3.2 EASE OF USE UNDER SIMULATED CONDITIONS

Ease of use was evaluated as a function of the number of steps required for a successful sample collection in a combination of possible situation encountered in the clinical setting. Both versions of our uterine collector were compared to the commercially available endometrial sampler TAO Brush®. Number of steps required for a successful sample collection were identified and registered with the combination of three situations. 1) No dilation aid required/no suction (minimum number of steps); 2) Dilation aid required; 3) Use of suction. Details for the test are provided in the table below (Table 4-8).

Table 4-8 — Test details: Ease of use under simulated conditions; step-count for sample collection.

Test Article	UC-A01	Collector Assembly
	UC-A02	Collector Assembly
	TAO Brush	Assembly
Parameters	Test conditions:	Simplified simulated use
	Test Temperature:	Room temperature. Usually between 20C to 25C
	Test Measure:	Number of steps required for sample collection
		Number of steps required for sample transfer to vial
Test end conditions	Test Measure	Step number

5 RESULTS

This chapter presents the results for the verification and validation tests used to establish safety and proof of concept. Section 5.1 presents structural and integrity testing; *In vitro* performance results are presented in section 5.2.

5.1 STRUCTURAL AND INTEGRITY TESTING

5.1.1 ADHESION STRENGTH: RISK OF FAILURE BY COMPONENT DISLODGEMENT

In pull-out experiments the force rose continuously with continuous extension of the sample to reach a maximum value taken as the pull-out force ***F***; Displacements at maximum force were recorded, as well as the failure mode. All tests were stopped once a steady decline in the measured force was observed.

5.1.1.1 COLLECTOR GUIDE (PULL-OUT) FORCE

The overall mean collector guide dislodgement force observed was 108 N (SD 13.81 N). The mean displacement at maximum force was 3.9 mm (SD 0.45 mm). As for specific failure cases, 14.3% of the samples were dislodged (93.5 N, SD 4.7 N; at 3.7 mm, SD 0.50 mm) while in 85.7% the collector guide yielded before being dislodged (110.3 N, SD 13.4 N; 3.9 mm, SD 0.5 mm). Table 5-1 shows the specific maximum forces reported, with displacements and failure modes for the dislodgement of the collector guide.

Figure 5-1 shows the force/displacement graphs for all the individual cases. Irregularities in the curves suggest that debonding began at a relatively low force of about 40 N, and the subsequent yield or dislodgement of the rubber collector guide from the metallic rod. *Figure* 5-2 shows the force/displacement curves for dislodgement cases.

Figure 5-3 shows the force/displacement curve for collector guide yield. Irregularities in the curves are consistent with different sites of debonding across the rubber-adhesive-metal interface. A longer plateau indicates the rubber deformation and eventual yield. Scattered data-points represent measured maximum pull-out forces.

Table 5-1 —Collector guide Dislodgement Force Test— Maximum force and mode of failure per specimen

Specimen	Max Force (N)	Mode of Failure	Specimen	Max Force (N)	Mode of Failure
1	106.7	Tip Yield	**16**	88.5	Dislodgement
2	102.9	Tip Yield	**17**	86.3	Tip Yield
3	100.56	Tip Yield	**18**	115.5	Tip Yield
4	114.2	Tip Yield	**19**	125	Tip Yield
5	107.23	Tip Yield	**20**	110	Tip Yield
6	98.5	Tip Yield	**21**	107.3	Tip Yield
7	90.5	Dislodgement	**22**	130.6	Tip Yield
8	105	Tip Yield	**23**	108.8	Tip Yield
9	111	Tip Yield	**24**	144.8	Tip Yield
10	98.3	Tip Yield	**25**	133.2	Tip Yield
11	125.5	Tip Yield	**26**	97.8	Dislodgement
12	104.9	Tip Yield	**27**	103.7	Tip Yield
13	97.2	Dislodgement	**28**	97.5	Tip Yield
14	97.4	Tip Yield	**Average**	**108**	
15	114.2	Tip Yield	**Std Dev**	**13.8**	

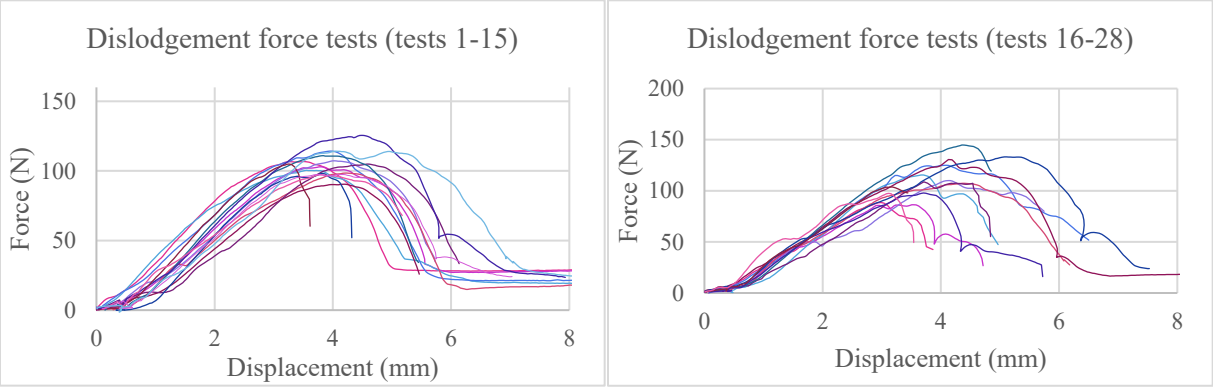

Figure 5-1 — Force-displacement graphs for specimens 1 to 15 (left) and 16-28 (right)— collector guide pull-out force.

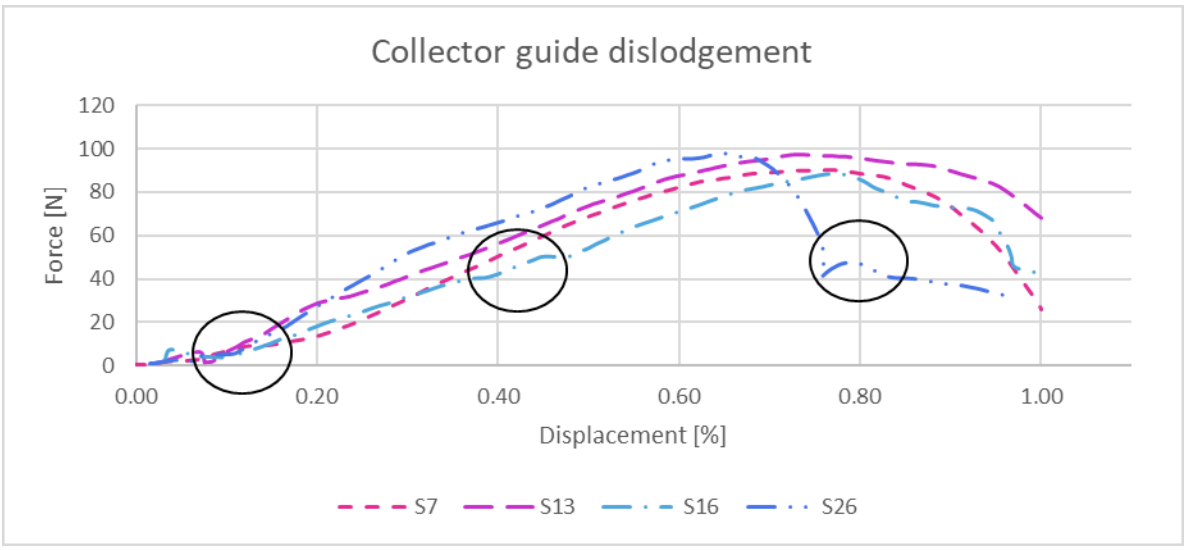

	S7	S13	S16	S26
Max force [N]	90.45	97.21	88.52	97.84
Max displacement [mm]	5.46	5.17	3.87	5.72

Figure 5-2 — Collector guide pull-out force/displacement curve for dislodgement cases. Circled areas show irregularities consistent with different sites of debonding across the rubber-adhesive-metal interface. Results are normalized for displacement. Maximum forces and displacements are shown. The tests were stopped once a decline in force was observed.

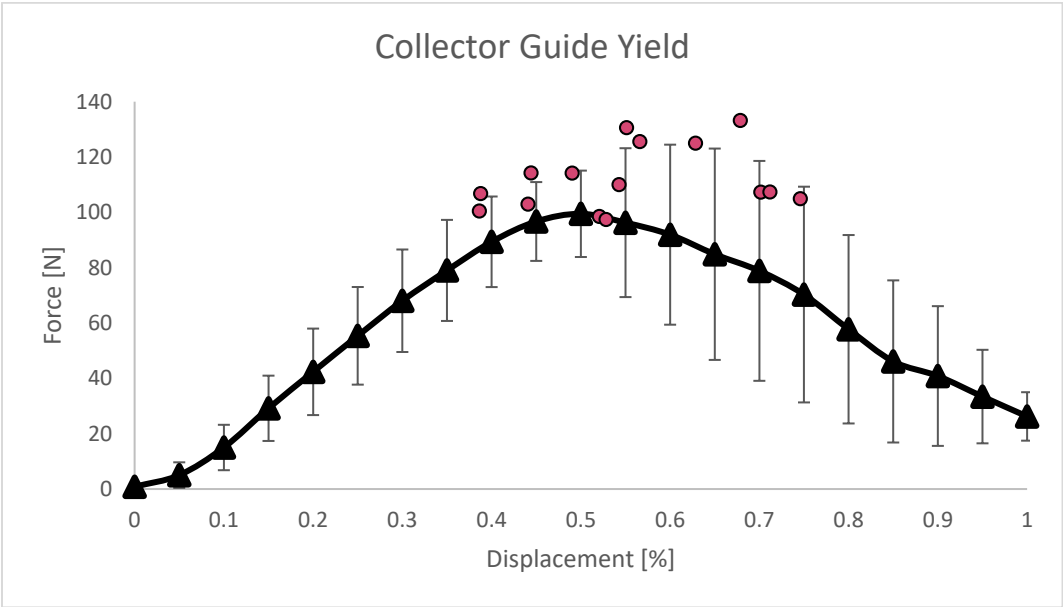

Figure 5-3 — Collector guide pull-out force/displacement curve for yield cases. The tests were stopped once a decline in force was observed. Irregularities in the curves are consistent with different sites of debonding across the rubber-adhesive-metal interface. A longer plateau indicates the rubber deformation and eventual yield. Scattered data points represent measured maximum pull-out forces. The solid line shows the mean force/displacement curve with error bars for standard deviation.

5.1.1.2 HANDLE PULL-OUT FORCE

The mean overall handle dislodgement force observed was 107.9 N ± 21.9 N. The mean displacement at maximum force was 1.6 ± 0.5 mm. All samples failed by dislodgment of the handle. Table 5-2 shows the specific maximum forces reported, with displacements for the dislodgement of the handle.

Table 5-2 — Handle dislodgement force test— Maximum force and displacement at handle dislodgement

Specimen	Max Force [N]	Displacement at F_{max} [mm]
S1	104.5	2.37
S2	156.1	1.68
S3	73.9	1.59
S4	108.4	1.2
S5	95.6	1.4
S6	111.2	2.4
S7	100.9	2
S8	129.1	1.1
S9	97.9	1.2
S10	100.9	1.4
AVERAGE	107.9	1.6
STD DEV	21.85	0.4

Figure 5-4 shows the force/displacement graphs for all the individual cases. Irregularities in the curves suggest the initial debonding began at relatively low forces of about 15-20 N, and the subsequent dislodgement of the plastic collector handle from the metallic rod.

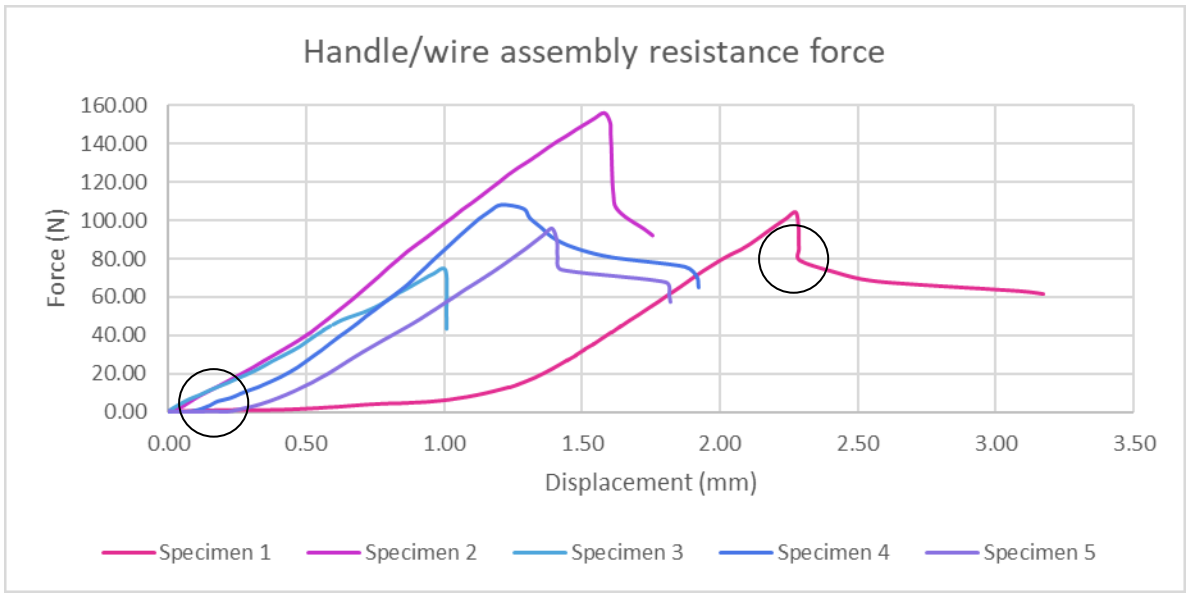

	S1	S2	S3	S4	S5
Max force [N]	104.50	156.06	73.87	108.42	95.64
Max displacement [mm]	3.17	1.76	1.01	1.92	1.82

Figure 5-4 — Handle dislodgement force for specimens 1 to 5. Maximum displacement values are shown for each sample, as well as maximum force.

5.1.1.3 SHEATH PULL-OUT FORCE

This test was designed to assess the quality of the valve/sheath assembly shown in Figure *4-7*. All samples showed yield of the sheath before debonding at the assembly site shown in Figure 5-5, with a mean maximum force of 56.8 N ± 2.2 N, and displacements before yield of 12.2 mm ± 0.5 mm, as shown in Figure 5-6. Table 5-3 shows detailed information per test specimen.

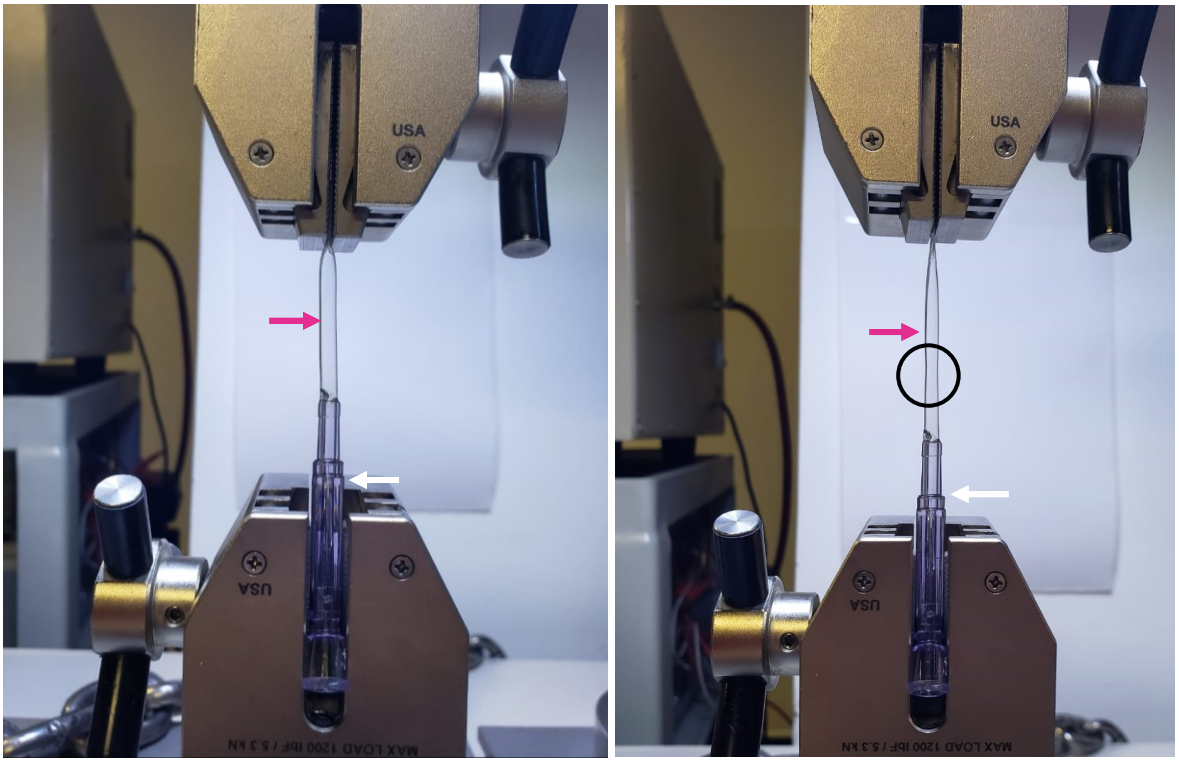

Figure 5-5 — Sheath Dislodgement, Instron ElectroPulsE1000. Collector Sheath (red arrow), Collector Valve (white arrow) — before (left) and after (right) testing. Note clear sheath yielding, circled in black.

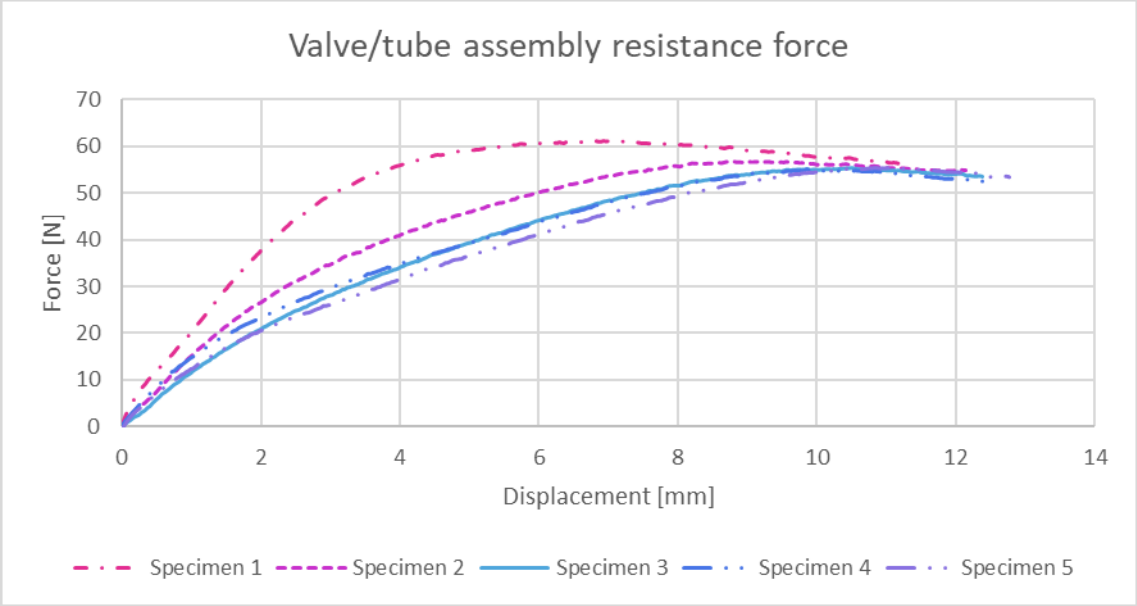

Figure 5-6 — Displacement–Dislodgement force graphs for specimens 1 to 5, sheath yield can be observed at a displacement of about 10-12 mm.

Table 5-3 — Sheath dislodgement force test— Maximum force/displacement per specimen

Specimen	Max Force [N]	Displacement at F max [mm]	Max Displacement [mm]
1	61.1	6.9	11.3
2	56.8	8.8	12.1
3	55.4	10.5	12.4
4	55.1	9.9	12.4
5	55.5	11.0	12.8
MEAN	**56.8**	**9.4**	**12.2**
STD DEV	**2.5**	**1.6**	**0.5**
STD. E. M.	**1.1**	**0.7**	**0.2**

5.1.2 FIBRE DISLODGEMENT ASSESSMENT

The observed probability of fibre dislodgement was zero. The combined probability of a device being used multiple times (event A) and of fibres being dislodged (event B) was 0.001. The probability of a device being used multiple times and its fibres not being dislodged was 0.099 and that of fibres being dislodged without the device being used several times as 0.009. The probability of a device being used as intended (single use) and there being no fibre dislodgement was 0.891. Figure 5-7 shows the Weibull cumulative distribution of failure/reliability for the use of the device as intended and the observed probability of failure.

Table 5-4 — Probabilistic analysis for fibre dislodgement. Observed and overweighed probabilities and calculated probabilities.

A	**Prob.**		**OWP***	**OP****		**OWP***	**OP****
Event A*	0.1	**P (A)^1**	0.1	0.1	**P (A)**	0.099	0.1
Event B*	0.01	**P (B)^1**	.01	0	**P (B)**	0.009	0
Event B**	0	**P ($A^1 \cap B^1$)**	.001	0	**P ((A∪ B)')**	0.891	0.9
* overweighed probability ** observed probability		**P ($A^1 \cup B^1$)**	0.109	0.1			
		P ($A^1 \Delta B^1$)	0.108	0.1			

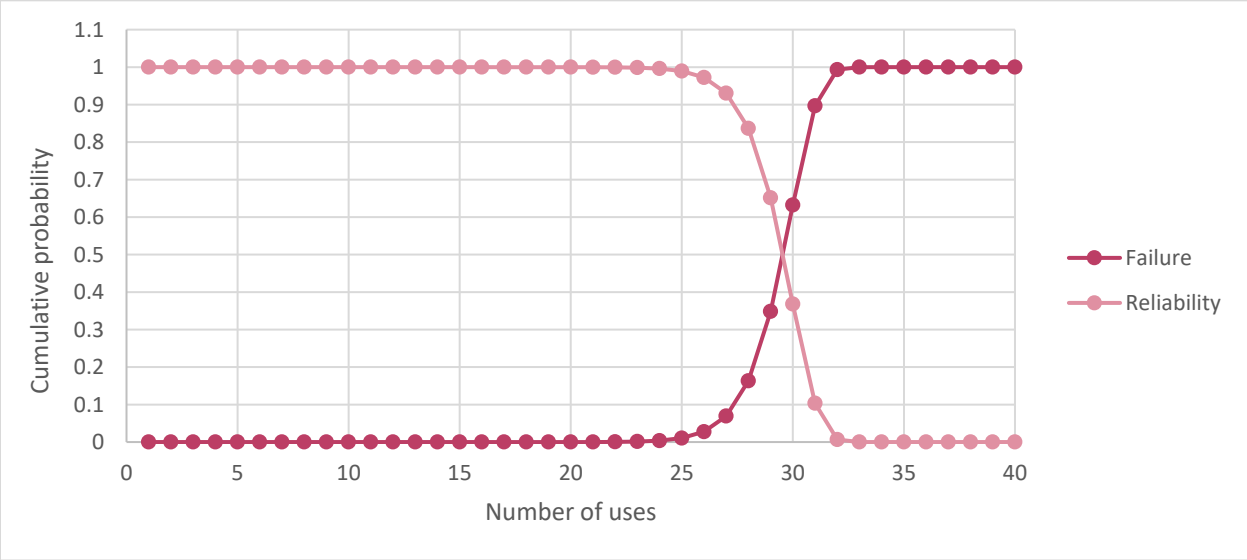

Figure 5-7 — Cumulative distribution of failure and device reliability for a single use device after repeated use with a safety factor of 30.

5.1.3 COMPRESSIVE STRENGTH AND RISK OF PERFORATION

All cases presented with device buckling or bowing without critical failure (bending/breaking). Case 1 (Table *4-6*) presented with the higher force required for buckling at 7.5 N. A critical load of 20 N [85]–[87], required to perforate the uterine tissue, was used to calculate the safety factor. The average force required for device insertion is shown in Table 3-1.

Table 5-5 — Column buckling analysis for compressive testing

Case	K	Force [N]	BLF	SF
1	0.5	7.5	0.4	2.7
2	1.0	3.5	0.2	5.7
3	0.707	4.8	0.5	4.2
4	2.0	6.7	0.3	3.0

5.2 IN VITRO PERFORMANCE

5.2.1 VOLUME COLLECTION

In simplified volume collection tests, the control device (TAO™ Brush), showed a mean collection volume of 600 µL ± 204 µL. The liquid biopsy devices A01 and A02 collected 643 µL ± 370 µL and 774 µL ± 151 µL, respectively. The mean transferred volumes were 320 µL ± 207 µL, 424 µL ± 347 µL, and 436 µL ± 160 µL for the control, collector A01 and collector A02 respectively. The designed collectors show an increase of 131% and 135% of transferred sample with respect to the control.

5.2.2 THEORETICAL PAIN ASSESSMENT

Radial force transferred to the cervical tissue for dilation, computed as a function of the taper of the dilation instrument used, and the longitudinal force show that at steeper dilation steps (ball-point), the radial pressure transferred to the cervical tissue is equivalent to the longitudinal force applied, while for a device with a taper angle of 4.76°, only about 68% of the longitudinal force is transferred radially. When looking at the rate of dilation, both profiles show a negative slope, with a 10-fold increase for the ball-point dilator compared to the 4.76° taper dilator (Figure 5-8).

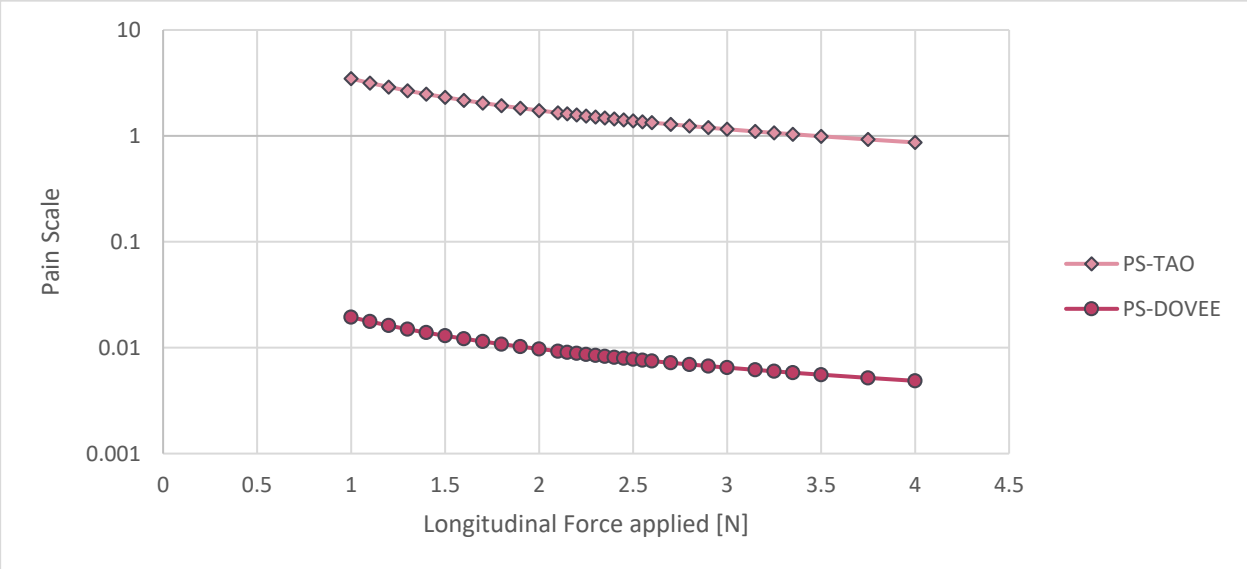

Figure 5-8 — Calculated pain scale based on device geometry and applied longitudinal force for insertion. Semi-logarithmic scale is used for better visualization.

5.2.3 EASE OF USE UNDER SIMULATED CONDITIONS

As mentioned in section 4.3.3, the number of steps required for a successful sample collection were identified and registered with the combination of three situations. 1) No dilation aid required/no suction (minimum number of steps); 2) Dilation aid required; 3) Use of suction.

The control device (TAO™ Brush) required a minimum of 14 steps out of 20 identified steps, from removal of the device from the package, to transfer of sample to a preservation vial. This increased to 19 when requiring external dilation aid. Both collectors UC-A01 and UC-A02 required 16 steps for sample collection with no dilation aid; 21 with dilation aid; and 19 to 20 for sample collection with use of suction functionality. Because the collector guide acts as an *os* dilator, the need of external dilation aid is not expected when using UC-A01 or UC-A02. The added steps are related to the deployment of the collection surface and use of suction. These can be further minimized with a redesign of the handle.

Table 5-6 — Steps identified for successful collection of uterine samples.

Device	No aid / no suction	External dilation	Suction
TAO ™ Brush	14	19	NA
UC-A01	16	21	19-20
UC-A02	16	21	19-20

5.2.4 THREE-DIMENSIONAL RECONSTRUCTION OF THE UTERINE CAVITY

A dimensional verification was performed on the solid models to ensure correlation with radiographic data (Table 5-7), the final model was in average 4% smaller in all dimensions than the measured MRI, due to the gap filling and smoothing filters applied after segmentation.

Table 5-7 — Dimensional verification of the solid models against radiographical data.

Structure	MRI	Solid	Model	%E (sol-MRI)	%E (mod-sol)	%E (mod-MRI)
Fundus	60.64	59.63	58.15	-2%	-2%	-4%
Uterine length	45.5	45.06	44.14	-1%	-2%	-3%
Cervical length	29.35	29.31	28.36	-0.14%	-3%	-3%
Cervical diameter	5.63	5.58	5.42	-1%	-3%	-4%

Figure 5-9 shows the segmentation label masks used to extract the anatomies of interest, and the resulting three-dimensional reconstruction. Figure 5-10 shows the obtained solid models, mold design and final physical silicone (ECOFLEX 00-10, Smooth-on Inc., PA) model, held open to allow for visualization of the uterine cavity. This model was intended to serve as an anatomically accurate and mechanically representative model for *in vitro* testing of design iterations for gynecological medical devices.

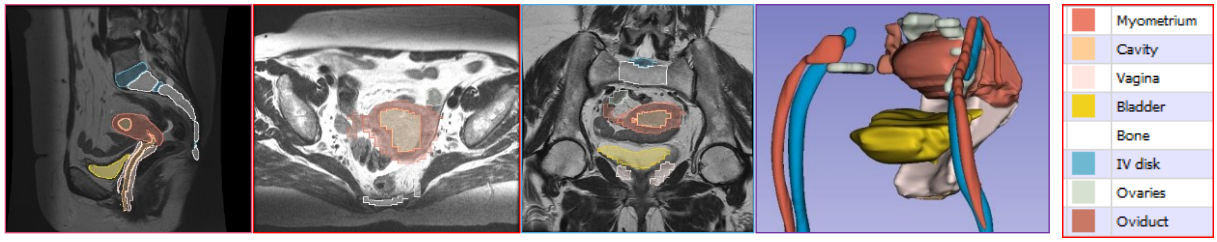

Figure 5-9 — Segmentation of the female pelvic organs. Left to right: sagittal, axial and coronal planes with overlaid segmentation labels, and 3D rendering of uterus (dark pink), uterine cavity, vagina (light pink), and surrounding anatomical references (bladder (yellow) and iliac vessels red and blue)).

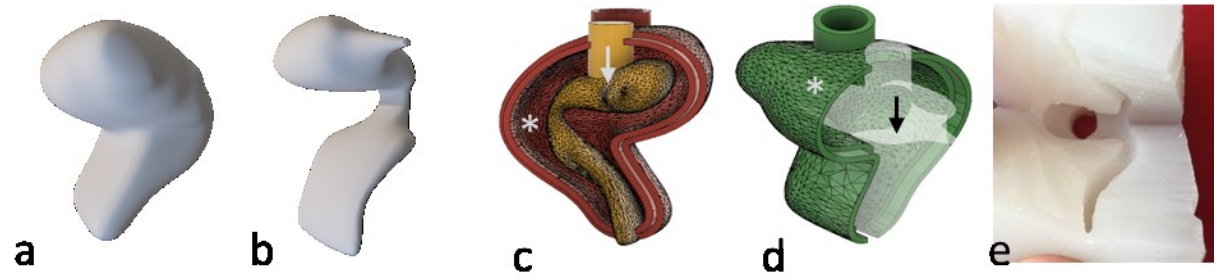

Figure 5-10 — Three-dimensional reconstruction of female pelvic organs. STL solids of the uterus (a) and uterine cavity (b); Mold assemblies for uterine sleeve/skin (c, d), uterine cavity (arrow), uterus (*) ; silicone rubber pelvic model held open for visualization of the uterine cavity (e).

6 DISCUSION

An initial approach to a liquid biopsy collector for the uterine cavity was generated for a simplified manufacturing process. Structural and integrity testing suggest that the devices will withstand their intended use, however, simplification of the design for a better physician experience and increase adoptability and ease of use are required.

STRUCTURAL INTEGRITY AND SAFETY

Collector guide —Irregularities observed along the curves in Figure 5-2 are consistent with the onset of debonding at specific sites. In Figure 5-1 and Figure 5-3 a temporary increase in force towards the end of the test, suggests the compression of the rubber polymeric chains providing an increase in resistance to pull-out. The variability in the results for dislodgement/yield can be attributed to variations in the application of adhesive and suggest variability in the manufacturing processes.

The longitudinal force needed for a cervical dilation ranges from 10 to 30 N for dilations in 10 mm steps[92],[93],[140]. This force decreases as the dilation diameter increases, giving the device a safety factor of at least 4. It is also important to note that the critical tensile direction occurs during the withdrawal of the device —when the cervix is already dilated to the device's maximum diameter (10 Fr / 3.3mm)—, making it highly unlikely for the tip to dislodge.

Although it may seem the selected geometry of the guide potentially increases the risk of uterine puncture, its dimensions and material properties have been selected to ensure it will bend before puncturing the tissue; the collector guide will bend at compressive loads of 1-4 N, well below the reported uterine puncture forces of 20 N [85],[131],[141].

Collector handle — This is a low-risk, non-patient-contacting component. The design control requirement was set to 50N, with a safety factor of at least 1.5. Failure of this component does not compromise functionality. Irregularities in the graph (Figure 5-4) may represent the initiation of debonding. After the maximum force, a drastic drop in forces can be observed, followed by a plateau, which may represent the frictional forces required to dislodge the handle from the rod after all adhesive bonds have been fractured. In this case, due to the properties of the handle material, no yielding is observed, and consequently, displacements are limited.

Outlier values (S2 and S3) can be explained by the variability of the assembly process. The pull-out force observed on S3 suggests there was no adhesive bonding between the two materials. Under standardized manufacturing processes and quality control assessment, it is expected that handle dislodgement would not occur.

Collector sheath — The valve/catheter assembly is handled as a single unit and not subject to tensile forces during intended use. The mode of failure was catheter yielding in all tests, with no dislodgement at all. As for the compressive forces, the component will bow under large compressive forces and may kink, but, the kinking does not constitute device failure and is noncritical to the overall performance.

Fibre dislodgement — Fibre dislodgement was assessed under highly unlikely assumptions, i.e. the probability of a single-use device being reused in the clinical setting. This scenario is unlikely due to current good clinical practice standards and regulations; also, the risk associated with the dislodgement of a fibre within the uterine cavity is minimal due to the material composition (medical grade nylon fibres). This material is also used for sutures, and on intrauterine devices, which can remain in the uterine cavity for up to 10 to 12 years.

PERFORMANCE

Volume collection — An increase in volume collection compared to the control was observed, which can be attributed either to the use of suction in the newer devices, or simply by the increase in the surface collection area available. Despite the fact that all devices were used following the same sequence of steps (

), a high variability in the results was observed. It should be noted that amongst all devices tested, UC-A02 was the more consistent both for volume collection and volume transfer.

The extra two steps required for the collection of samples using the new devices seems a fair trade-off when considering the increase in volume collection and transfer. This metric can be further improved with a redesign of the handle, to remove the requirement of the valve. A trade-off between ease of use and functional features might be necessary.

Pain assessment — Although pain is subjective, a correlation between insertion forces, resistance to dilation and deformation can be helpful to objectively assess and compare different technologies. We obtained a scale of the radial force transmitted to the cervical tissue with a

given longitudinal force, and it became apparent, that regardless of the longitudinal force applied, the dilation rate plays a more important role in tissue deformation and rupture. A simple method to predict pain is the correlation between the radial dilation and longitudinal length of insertion or device taper angle. So a smooth incremental dilation with a lower strain rate would induce less trauma and pain to the tissue than a blunt dilation step. [140]

Model — The generation of computational and physical models, representative of all stages in the female reproductive cycle are required for the safe evaluation of new technologies as well as elucidating the mechanical processes involved in the onset of disease.

Automated segmentation of complex structures is often not achievable and requires user intervention. Because of this, some segmentation algorithms have been developed[115],[142],[143], to aid in the identification of structures across slices applying filters or allowing for the propagation of delineated images or atlases which can in turn be used with machine learning applications[105].

Although this model was generated using silicones due to their durability, high shelf life and relatively easy and quick curing time, while obtaining properties as close to those reported in the literature as possible, other materials like hydrogels (PVA, chitosan, alginate, etc.) could be more suitable for better biomechanical representation, but their use presents particular manufacturing challenges, related specifically to the cross-linking of the polymeric chains.

Further work is required to streamline the process from medical imaging to biomechanical models. The use of machine learning together with the development of bio inks, or new cross-linking methods for hydrogels, could potentially facilitate the generation of patient-specific, biomechanically compatible engineered models. These fine-tuned mock-ups could be useful in the assessment of new technologies, surgical training and planning, and tissue engineering.

Women around the globe lack access to gynecological health due to varied socio-economical and cultural barriers. With this in mind, the use of self-sampling devices for cervical cancer (Papanicolaou test), and sexually transmitted diseases has been studied for non-inferiority compared to sample collection in the clinical setting[144],[145]; if adopted, these self-sampling devices could improve the health of millions of women worldwide, hence the feasibility of the transformation of this intrauterine sampler into a self-collection device should be explored.

7 CONCLUSION

This thesis presents the design of a device for intrauterine liquid biopsy sample collection and analyses the structural integrity and performance of such a device. The proof of concept was validated *in vitro* and rendered a structurally sound, safe and effective device, yet to be tested in clinical trials beyond the scope of this work.

Mechanical characterization of the female reproductive tissues has been greatly limited to its relevance towards human reproduction. Ethical considerations limit the access to these tissues for full mechanical characterization, this fact together with the cyclic nature of the tissues and the lack of standardized testing protocols, render the data available in the literature highly variable and inconclusive, leaving an important gap in the understanding of the role of biomechanically induced changes in the onset and pathophysiology of disease.

Further improvement of the design is required, including the combination of simplified use and added functionalities, and the testing and validation of the design changes. The feasibility of the transformation into a self-collection device should also be considered.

REFERENCES

[1] The American Cancer Society. Key Statistics for Ovarian Cancer. https://www.cancer.org/cancer/ovarian-cancer/about/key-statistics.html (2018).

[2] The American Cancer Society. Cancer Facts & Statistics. *Cancer Statistics Center* https://cancerstatisticscenter.cancer.org/?_ga=2.251664521.107294489.1550068454-2070538720.1550068454#!/ (2018).

[3] Ovarian Cancer Reseach Alliance. Statistics - Ovarian Cancer Research Alliance. https://ocrahope.org/patients/about-ovarian-cancer/statistics/.

[4] Canadian Cancer Society's Advisory Committee on Cancer Statistics. Ovarian Cancer Statistics. *Canadian Cancer Statistics* http://www.cancer.ca/en/cancer-information/cancer-type/ovarian/statistics/?region=on (2017).

[5] Siegel, R. L., Miller, K. D. & Jemal, A. Cancer statistics, 2017. *CA. Cancer J. Clin.* **67**, 7–30 (2017).

[6] Ferlay, J., Soerjomataram, I., Dikshit, R., Eser, S., Mathers, C., Rebelo, M., Parkin, D. M., Forman, D. & Bray, F. Cancer incidence and mortality worldwide: sources, methods and major patterns in GLOBOCAN 2012. *Int. J. cancer* **136**, E359-86 (2015).

[7] Antoni, S., Soerjomataram, I., Møller, B., Bray, F. & Ferlay, J. An assessment of GLOBOCAN methods for deriving national estimates of cancer incidence. *Bull. World Health Organ.* **94**, 174–184 (2016).

[8] Canadian Cancer Society's Advisory Committee on Cancer Statistics. Uterine cancer statistics. *Canadian Cancer Statistics 2019* https://www.cancer.ca/en/cancer-information/cancer-type/uterine/statistics/?region=on#:~:targetText=Incidence and mortality&targetText=An estimated 7%2C200 Canadian women,will die from the disease. (2019).

[9] The American Cancer Society. Key Statistics for Endometrial Cancer. https://www.cancer.org/cancer/endometrial-cancer/about/key-statistics.html (2018).

[10] Canadian Cancer Society's Advisory Committee on Cancer Statistics. Canadian Cancer Statistics 2019. 95 cancer.ca/Canadian-Cancer-Statistics-2019-EN (2019).

[11] Surveillance Research Program (National Cancer Institute). Cancer Stat Facts: Uterine Cancer. *SEER*Explorer* https://seer.cancer.gov/statfacts/html/corp.html.

[12] World Cancer Research Fund. Endometrial (womb) cancer | World Cancer Research Fund International. https://www.wcrf.org/dietandcancer/endometrial-cancer.

[13] Bray, F., Ferlay, J., Soerjomataram, I., Siegel, R. L., Torre, L. A. & Jemal, A. Global cancer statistics 2018: GLOBOCAN estimates of incidence and mortality worldwide for 36 cancers in 185 countries. *CA. Cancer J. Clin.* **68**, 394–424 (2018).

[14] World Health Organization. Burden of Disease -Disease and injury country estimates. *Health Statistics and Information systems* https://www.who.int/healthinfo/global_burden_disease/estimates_country/en/ (2014).

[15] Kearns, B., Chilcott, J., Whyte, S., Preston, L. & Sadler, S. Cost-effectiveness of screening for ovarian cancer amongst postmenopausal women: a model-based economic evaluation. *BMC Med.* **14**, 200 (2016).

[16] Moss, H. A., Berchuck, A., Neely, M. L., Myers, E. R. & Havrilesky, L. J. Estimating Cost-effectiveness of a Multimodal Ovarian Cancer Screening Program in the United States: Secondary Analysis of the UK Collaborative Trial of Ovarian Cancer Screening (UKCTOCS). *JAMA Oncol.* **4**, 190–195 (2018).

[17] Kinde, I., Bettegowda, C., Wang, Y., Wu, J., Agrawal, N., Shih, I. M., Kurman, R., Dao, F., Levine, D. A., Giuntoli, R., Roden, R., Eshleman, J. R., Carvalho, J. P., Marie, S. K. N., Papadopoulos, N., Kinzler, K. W., Vogelstein, B. & Diaz, L. A. Evaluation of DNA from the papanicolaou test to detect ovarian and endometrial cancers. *Sci. Transl. Med.* **5**, (2013).

[18] Maritschnegg, E., Wang, Y., Pecha, N., Horvat, R., Van Nieuwenhuysen, E., Vergote, I., Heitz, F., Sehouli, J., Kinde, I., Diaz, L. A., Papadopoulos, N., Kinzler, K. W., Vogelstein, B., Speiser, P. & Zeillinger, R. Lavage of the uterine cavity for molecular detection of Müllerian duct carcinomas: A proof-of-concept study. *J. Clin. Oncol.* **33**, 4293–4300 (2015).

[19] Nair, N., Camacho-Vanegas, O., Rykunov, D., Dashkoff, M., Camacho, S. C., Schumacher, C. A., Irish, J. C., Harkins, T. T., Freeman, E., Garcia, I., Pereira, E., Kendall, S., Belfer, R., Kalir, T., Sebra, R., Reva, B., Dottino, P. & Martignetti, J. A. Genomic Analysis of Uterine Lavage Fluid Detects Early Endometrial Cancers and Reveals a Prevalent Landscape of Driver Mutations in Women without Histopathologic Evidence of Cancer: A Prospective Cross-Sectional Study. *PLOS Med.* **13**, e1002206 (2016).

[20] Wang, Y., Li, L., Douville, C., Cohen, J. D., Yen, T.-T., Kinde, I., Sundfelt, K., Kjær, S. K., Hruban, R. H., Shih, I.-M., Wang, T.-L., Kurman, R. J., Springer, S., Ptak, J., Popoli, M., Schaefer, J., Silliman, N., Dobbyn, L., Tanner, E. J., et al. Evaluation of liquid from the Papanicolaou test and other liquid biopsies for the detection of endometrial and ovarian cancers. *Sci. Transl. Med.* **10**, eaap8793 (2018).

[21] Temkin, S. M., Gregory, T., Kohn, E. C. & Duska, L. Gynecology. in *Schwartz's Principles of Surgery, 11e* (eds. Brunicardi, F. C., Andersen, D. K., Billiar, T. R., Dunn, D. L., Kao, L. S., Hunter, J. G., Matthews, J. B. & Pollock, R. E.) (McGraw-Hill Education, 2019).

[22] Uterus. *Encyclopedia Britannica* (2019).

[23] Snell, R. Clinical Anatomy by systems. in *Annals of surgery* (2002).

[24] HEINTZ, A., ODICINO, F., MAISONNEUVE, P., QUINN, M., BENEDET, J., CREASMAN, W., NGAN, H., PECORELLI, S. & BELLER, U. Carcinoma of the Ovary. *Int. J. Gynecol. Obstet.* **95**, S161–S192 (2006).

[25] Clift, A. F. & Hart, J. VARIATIONS IN THE APPARENT VISCOSITY OF HUMAN CERVICAL MUCUS. *J. Physiol* **122**, 358–365 (1953).

[26] Wolf, D. P., Blasco, L., Khan, M. A. & Litt, M. Human Cervical Mucus. I. Rheologic Characteristics. *Fertil. Steril.* **28**, 41–46 (1977).

[27] Wolf, D. P., Blasco, L., Khan, M. A. & Litt, M. Human Cervical Mucus. II. Changes in Viscoelasticity During the Ovulatory Menstrual Cycle. *Fertil. Steril.* **28**, 47–52 (1977).

[28] Karni, Z., Polishuk, W. Z., Adoni, A. & Diamant, Y. Newtonian viscosity of the human cervical mucus during the menstrual cycle. *Obstetrical and Gynecological Survey* vol. 27 689–690 (1972).

[29] Ding, D., Shi, W. & Shi, Y. Numerical simulation of embryo transfer: How the viscosity of transferred medium affects the transport of embryos. *Theor. Biol. Med. Model.* **15**, 5–7 (2018).

[30] Allen, W. R., Tiplady, C. A., Butler, S. & Mackley, M. R. Rheological characterisation of estrous uterine fluid in the mare. *Theriogenology* **58**, 503–506 (2002).

[31] Roberts, G. P., Parker, J. M. & Henderson, S. R. Proteins in human uterine fluid. *J. Reprod. Fertil.* **48**, 153–157 (1976).

[32] Debby, A., Malinger, G., Glezerman, M. & Golan, A. Intra-uterine fluid collection in postmenopuasal women with cervical stenosis. *Maturitas* **55**, 334–337 (2006).

[33] Clift, A. F. Early studies on the rheology of cervical mucus. *Am. J. Obstet. Gynecol.* **134**, 829–832 (1979).

[34] Myers, K. M. & Elad, D. Biomechanics of the human uterus. *Wiley Interdiscip. Rev. Syst. Biol. Med.* **9**, e1388 (2017).

[35] Ross, M. & Pawlina, W. Histology: A Text and Atlas, with Correlated Cell and Molecular Biology, 6th Edition. in *Histology: A Text and Atlas* (2010).

[36] Jiménez-Ayala, M. & Jiménez-Ayala, B. Cytology of the Normal Endometrium – Cycling and Postmenopausal. in *Endometrial Adenocarcinoma: Prevention and Early Diagnosis* 32–39 (KARGER, 2008). doi:10.1159/000117494.

[37] Ross, M. H. & Pawlina, W. Female Reproductive System. in *Histology: A Text and Atlas: With correlated cell and molecular biology* 974 (Wolters Kluwer / Lippincott Williams & Wilkings Health, 2011).

[38] Leppert, P. C. & Yu, S. Y. Three-dimensional structures of uterine elastic fibers: Scanning electron microscopic studies. *Connect. Tissue Res.* (1991) doi:10.3109/03008209109006992.

[39] Myers, K. M., Paskaleva, A. P., House, M. & Socrate, S. Mechanical and biochemical properties of human cervical tissue. *Acta Biomater.* **4**, 104–116 (2008).

[40] Vink, J. Y., Qin, S., Brock, C. O., Zork, N. M., Feltovich, H. M., Chen, X., Urie, P., Myers, K. M., Hall, T. J., Wapner, R., Kitajewski, J. K., Shawber, C. J. & Gallos, G. A new paradigm for the role of smooth muscle cells in the human cervix. in *American Journal of Obstetrics and Gynecology* vol. 215 478.e1-478.e11 (Mosby Inc., 2016).

[41] Arangio, G. A., Bae, K. H., Kim, J. W. J. Y., Kim, T. K., Kweon, S. H., Kang, H. J., Kim, J. W. J. Y., Joo, M. S., Kim, D. M., Benjamin, M., Ralphs, J. R., Buschmann, J., Meier Bürgisser, G., Jordan, M. C., Schmitt, V., Jansen, H., Meffert, R. H., Hoelscher-Doht, S., Kummer, F., et al. Minimal mechanical load and tissue culture conditions preserve native cell phenotype and morphology in tendon-a novel ex vivo mouse explant model. *J. Anat* **25**, 611–616 (2011).

[42] DANFORTH, D. N. The distribution and functional activity of the cervical musculature. *Am. J. Obstet. Gynecol.* **68**, 1261–71 (1954).

[43] Vink, J. & Myers, K. Cervical alterations in pregnancy. *Best Practice and Research: Clinical Obstetrics and Gynaecology* vol. 52 88–102 (2018).

[44] Coy Fuster, P., Avilés, M. & Latorre Reviriego, R. Fallopian Tube/Oviduct. *Encycl. Reprod.* 276–281 (2018) doi:10.1016/B978-0-12-801238-3.64400-8.

[45] House, M., Kaplan, D. L. & Socrate, S. Relationships Between Mechanical Properties and Extracellular Matrix Constituents of the Cervical Stroma During Pregnancy. *Seminars in Perinatology* vol. 33 300–307 (2009).

[46] Timraz, S. B. H., Rezgui, R., Boularaoui, S. M. & Teo, J. C. M. Stiffness of extracellular matrix components modulates the phenotype of human smooth muscle cells in vitro and allows for the control of properties of engineered tissues. *Procedia Eng.* **110**, 29–36 (2015).

[47] Fung, Y.-C. *Biomechanics Mechanical Properties of Living Tissues*. (Springer New York, 1993). doi:10.1007/978-1-4757-2257-4.

[48] Rauh-Hain, J. a, Krivak, T. C., Del Carmen, M. G. & Olawaiye, A. B. Ovarian cancer screening and early detection in the general population. *Rev. Obstet. Gynecol.* **4**, 15–21 (2011).

[49] Segal, T. R. & Abittan, B. S. Premalignant & Malignant Disorders of the Ovaries & Oviducts. in *CURRENT Diagnosis & Treatment: Obstetrics & Gynecology, 12e* (eds. DeCherney, A. H., Nathan, L., Laufer, N. & Roman, A. S.) (McGraw-Hill Education, 2019).

[50] Baskovic, M. & Dorigo, O. Premalignant & Malignant Disorders of the Uterine Corpus. in *CURRENT Diagnosis & Treatment: Obstetrics & Gynecology, 12e* (eds. DeCherney, A. H., Nathan, L., Laufer, N. & Roman, A. S.) (McGraw-Hill Education, 2019).

[51] Uterine cancer survival statistics | Cancer Research UK. https://www.cancerresearchuk.org/health-professional/cancer-statistics/statistics-by-cancer-type/uterine-cancer/survival#heading-Three.

[52] Fathalla, M. F. Factors in the causation and incidence of ovarian cancer. *Obstetrical and Gynecological Survey* vol. 27 751–768 (1972).

[53] Auersperg, N., Wong, A. S. T., Choi, K. C., Kang, S. K. & Leung, P. C. K. Ovarian surface epithelium: Biology, endocrinology, and pathology. *Endocr. Rev.* **22**, 255–288 (2001).

[54] Auersperg, N., Edelson, M. I., Mok, S. C., Johnson, S. W. & Hamilton, T. C. The biology of ovarian cancer. *Semin. Oncol.* **25**, 281–304 (1998).

[55] Lengyel, E. Ovarian cancer development and metastasis. *American Journal of Pathology* vol. 177 1053–1064 (2010).

[56] Goff, B. A., Mandel, L. S., Drescher, C. W., Urban, N., Gough, S., Schurman, K. M., Patras, J., Mahony, B. S. & Andersen, M. R. Development of an ovarian cancer symptom index. *Cancer* **109**, 221–227 (2007).

[57] Dearking, A. C., Aletti, G. D., McGree, M. E., Weaver, A. L., Sommerfield, M. K. & Cliby, W. A. How relevant are ACOG and SGO guidelines for referral of adnexal mass? *Obstet. Gynecol.* **110**, 841–848 (2007).

[58] Baskovic, M. & Dorigo, O. Premalignant & Malignant Disorders of the Uterine Corpus | CURRENT Diagnosis & Treatment: Obstetrics & Gynecology, 12e | AccessMedicine | McGraw-Hill Medical. in *Current Diagnosis & Treatment*.

[59] Berek, J. S. & Hacker, N. F. Ovarian Cancer. in *Becrek and Hacker's Gynecologic Oncology* (Wolters Kluwer, 2014).

[60] Pinsky, P. F., Yu, K., Kramer, B. S., Black, A., Buys, S. S., Partridge, E., Gohagan, J., Berg, C. D. & Prorok, P. C. Extended Mortality Results for Ovarian Cancer Screening in the PLCO Trial with Median 15 Years Follow-up. doi:10.1016/j.ygyno.2016.08.334.

[61] Henderson, J. T., Webber, E. M. & Sawaya, G. F. Screening for ovarian cancer updated evidence report and systematic review for the US preventive services task force. *JAMA - J. Am. Med. Assoc.* **319**, 595–606 (2018).

[62] Pennington, M., Gentry-Maharaj, A., Karpinskyj, C., Miners, A., Taylor, J., Manchanda, R., Iyer, R., Griffin, M., Ryan, A., Jacobs, I., Menon, U. & Legood, R. Long-Term Secondary Care Costs of Endometrial Cancer: A Prospective Cohort Study Nested within the United Kingdom Collaborative Trial of Ovarian Cancer Screening (UKCTOCS). *PLoS One* **11**, e0165539 (2016).

[63] Fields, M. M. & Chevlen, E. Ovarian Cancer Screening: A Look at the Evidence. *Clin. J. Oncol. Nurs.* **10**, 77–81 (2006).

[64] Tumor Markers | SEER Training. https://training.seer.cancer.gov/ovarian/abstract-code-stage/extent/markers.html.

[65] Soeters, R., Whittaker, J. & Dehaeck, K. Endometrial sampling: a comparison between the Pipelle ® endometrial sampler and the Endosampler ®. *South. African J. Gynaecol. Oncol.* **3**, 34–38 (2011).

[66] Ilié, M. & Hofman, P. Pros: Can tissue biopsy be replaced by liquid biopsy? *Transl. lung cancer Res.* **5**, 420–3 (2016).

[67] Sato, Y., Matoba, R. & Kato, K. Recent Advances in Liquid Biopsy in Precision Oncology Research. *Biol.*

Pharm. Bull. **42**, 337–342 (2019).

[68] Jung, A. & Kirchner, T. Liquid Biopsy in Tumor Genetic Diagnosis. *Dtsch. Arztebl. Int.* **115**, 169–174 (2018).

[69] Neumann, M. H. D., Bender, S., Krahn, T. & Schlange, T. ctDNA and CTCs in Liquid Biopsy – Current Status and Where We Need to Progress. *Comput. Struct. Biotechnol. J.* **16**, 190–195 (2018).

[70] Wang, Y., Li, L., Douville, C., Cohen, J. D., Yen, T. T., Kinde, I., Sundfelt, K., Kjær, S. K., Hruban, R. H., Shih, I. M., Wang, T. L., Kurman, R. J., Springer, S., Ptak, J., Popoli, M., Schaefer, J., Silliman, N., Dobbyn, L., Tanner, E. J., et al. Evaluation of liquid from the Papanicolaou test and other liquid biopsies for the detection of endometrial and ovarian cancers. *Sci. Transl. Med.* **10**, (2018).

[71] Giannopoulou, L., Zavridou, M., Kasimir-Bauer, S. & Lianidou, E. S. Liquid biopsy in ovarian cancer: the potential of circulating miRNAs and exosomes. *Transl. Res.* **205**, 77–91 (2019).

[72] Kawahara, A., Fukumitsu, C., Taira, T., Abe, H., Takase, Y., Murata, K., Yamaguchi, T., Azuma, K., Ishii, H., Takamori, S., Akiba, J., Hoshino, T. & Kage, M. Epidermal growth factor receptor mutation status in cell-free DNA supernatant of bronchial washings and brushings. *Cancer Cytopathol.* **123**, 620–628 (2015).

[73] De Mattos-Arruda, L., Mayor, R., Ng, C. K. Y., Weigelt, B., Martínez-Ricarte, F., Torrejon, D., Oliveira, M., Arias, A., Raventos, C., Tang, J., Guerini-Rocco, E., Martínez-Saéz, E., Lois, S., Marín, O., De La Cruz, X., Piscuoglio, S., Towers, R., Vivancos, A., Peg, V., et al. Cerebrospinal fluid-derived circulating tumour DNA better represents the genomic alterations of brain tumours than plasma. *Nat. Commun.* **6**, (2015).

[74] Millholland, J. M., Li, S., Fernandez, C. A. & Shuber, A. P. Detection of low frequency FGFR3 mutations in the urine of bladder cancer patients using next-generation deep sequencing. *Open Access J. Urol.* **4**, 33–40 (2012).

[75] Clark, J. T. & Gupta, J. K. Endometrial sampling of gynaecological pathology. *Obstet. Gynaecol.* **4**, 169–174 (2002).

[76] Lipscomb, G. H., Lopatine, S. M., Stovall, T. G. & Ling, F. W. A randomized comparison of the Pipelle, Accurette, and Explora endometrial sampling devices. *Am. J. Obstet. Gynecol.* **170**, 591–594 (1994).

[77] Baah-Dwomoh, A., McGuire, J., Tan, T. & De Vita, R. Mechanical Properties of Female Reproductive Organs and Supporting Connective Tissues: A Review of the Current State of Knowledge. *Appl. Mech. Rev.* **68**, 060801 (2016).

[78] Chanda, A., Unnikrishnan, V., Roy, S. & Richter, H. E. Computational Modeling of the Female Pelvic Support Structures and Organs to Understand the Mechanism of Pelvic Organ Prolapse: A Review. *Applied Mechanics Reviews* (2015) doi:10.1115/1.4030967.

[79] Conrad, J. T., Johnson, W. L., Kuhn, W. K. & Hunter, C. A. Passive stretch relationships in human uterine muscle. *Am. J. Obstet. Gynecol.* **96**, 1055–1059 (1966).

[80] Conrad, J. T. & Kuhn, W. The active length-tension relationship in human uterine muscle. *Am. J. Obstet. Gynecol.* **97**, 154–160 (1967).

[81] Pearsall, G. W. & Roberts, V. L. Passive mechanical properties of uterine muscle (myometrium) tested in vitro. *J. Biomech.* **11**, 167–176 (1978).

[82] Kauer, M., Vuskovic, V., Dual, J., Szekely, G. & Bajka, M. Inverse finite element characterization of soft tissues. *Med. Image Anal.* **6**, 275–287 (2002).

[83] Manoogian, S. J., Bisplinghoff, J. A., Kemper, A. R. & Duma, S. M. Dynamic material properties of the pregnant human uterus. *J. Biomech.* **45**, 1724–1727 (2012).

[84] Manoogian, S. J., Mcnally, C., Stitzel, J. D. & Duma, S. M. Dynamic Biaxial Tissue Properties of Pregnant Porcine Uterine Tissue. *Stapp Car Crash J.* **52**, 167–185 (2008).

[85] Goldstuck, N. D. Insertion forces with intrauterine devices: implications for uterine perforation. *Eur. J. Obstet. Gynecol. Reprod. Biol.* **25**, 315–323 (1987).

[86] Goldstuck, N. & Wildemeersch, D. Role of uterine forces in intrauterine device embedment, perforation, and expulsion. *Int. J. Womens. Health* **6**, 735 (2014).

[87] Turok, D. K., Cappiello, B., Sanders, J. N., Royer, P. A., Thompson, I. & Gawron, L. M. Ex-vivo forces associated with IUD insertion and perforation: biomechanical evaluation of hysterectomy specimens. *Contraception* **92**, 379–380 (2015).

[88] Mazza, E., Nava, A., Bauer, M., Winter, R., Bajka, M. & Holzapfel, G. A. Mechanical properties of the human uterine cervix: An in vivo study. *Med. Image Anal.* **10**, 125–136 (2006).

[89] Yao, W., Yoshida, K., Fernandez, M., Vink, J., Wapner, R. J., Ananth, C. V., Oyen, M. L. & Myers, K. M. Measuring the compressive viscoelastic mechanical properties of human cervical tissue using indentation. *J. Mech. Behav. Biomed. Mater.* **34**, 18–26 (2014).

[90] Young, B. W. & Craven, A. H. Force-dilatation characteristics of the human cervix. *Med. Biol. Eng. Comput.* **15**, 280–291 (1977).

[91] Nicolaides, K. H., Welch, C. C., Pherson, M. B. A. M., Johnson, I. R. & Filshie, G. M. Lamicel: a new technique for cervical dilatation before first trimester abortion. *BJOG An Int. J. Obstet. Gynaecol.* **90**, 475–479 (1983).

[92] ANTHONY, G. S., FISHER, J., COUTTS, J. R. T. & CALDER, A. A. Forces required for surgical dilatation of the pregnant and non-pregnant human cervix. *BJOG An Int. J. Obstet. Gynaecol.* **89**, 913–916 (1982).

[93] Fisher, J., Anthony, G. S., Mcmanus, T. J., Coutts, J. R. T. & Calder, A. A. Use of a force measuring instrument during cervical dilatation. *J. Med. Eng. Technol.* **5**, 194–195 (1981).

[94] ANTHONY, G. S., CALDER, A. A. & MACNAUGHTON, M. C. Cervical resistance in patients with

previous spontaneous mid-trimester abortion. *BJOG An Int. J. Obstet. Gynaecol.* **89**, 1046–1049 (1982).

[95] Goldstuck, N. D. 'Bowing' forces with IUD inserters in vitro: relevance to difficult IUD insertions. *Clin. Reprod. Fertil.* **5**, 173–6 (1987).

[96] Jobling, P., O'Hara, K. & Hua, S. Female reproductive tract pain: Targets, challenges, and outcomes. *Frontiers in Pharmacology* vol. 5 FEB (2014).

[97] Tingaker, B. K., Ekman-Ordeberg, G. & Forsgren, S. Presence of sensory nerve corpuscles in the human corpus and cervix uteri during pregnancy and labor as revealed by immunohistochemistry. *Reprod. Biol. Endocrinol.* **4**, (2006).

[98] Goldstuck, N. D. Pain reduction during and after insertion of an intrauterine contraceptive device. *Adv. Contracept.* **3**, 25–36 (1987).

[99] Eytan, O., Zaretsky, U., Jaffa, A. J., Elad, D., Kissler, S., Hamscho, N., Zangos, S., Wiegratz, I., Doebert, N., Gruenwald, F., Vogl, T. J., Siebzehnruebl, E., Leyendecker, G. & Kaufmann, M. Simulations of embryo transfer procedures with a laboratory uterine model Utero-tubal transport disorder in adenomyosis and endometriosis-a cause for infertility. in *Reproductive Biomechanics*.

[100] Gonçalves, A. D., Alexander, C., Roberts, C. J., Spain, S. G., Uddin, S. & Allen, S. The effect of protein concentration on the viscosity of a recombinant albumin solution formulation. *RSC Adv.* **6**, 15143–15154 (2016).

[101] Karni, Z., Polishuk, W. Z., Adoni, A. & Diamant, Y. Newtonian viscosity of the human cervical mucus during the menstrual cycle. *International Journal of Fertility* vol. 16 185–188 (1971).

[102] Clift, A. F. & Hart, J. VARIATIONS IN THE APPARENT VISCOSITY OF HUMAN CERVICAL MUCUS. *J. Physiol* **122**, 358–365 (1953).

[103] Ibrahim, E.-S. H. & Osman, N. F. Magnetic Resonance Imaging. in *Handbook of Physics in Medicine and Biology* (ed. Splinter, R.) 28:1–18 (CRC Press, 2010). doi:10.1201/9781420075250.

[104] Runge, V. M., Nitz, W. R. & Heverhagen, J. T. Image Resolution: Pixel and Voxel Size. in *The Physics of clinical MR Taught Through Images* (eds. Runge, V. M., Nitz, W. R. & Heverhagen, J. T.) 34–36 (Thieme Publishers New York, 2018). doi:10.1055/b-006-160181.

[105] Iglesias, J. E. & Sabuncu, M. R. Multi-atlas segmentation of biomedical images: A survey. *Med. Image Anal.* **24**, 205–219 (2015).

[106] Yushkevich, P. A., Piven, J., Hazlett, H. C., Smith, R. G., Ho, S., Gee, J. C. & Gerig, G. User-guided 3D active contour segmentation of anatomical structures: Significantly improved efficiency and reliability. *Neuroimage* **31**, 1116–1128 (2006).

[107] Zara, F. & Dupuis, O. Uterus – Biomechanical modeling of uterus. Application to a childbirth simulation. *Biomech. Living Organs Hyperelastic Const. Laws Finite Elem. Model.* (2017).

[108] Chepelev, L., Wake, N., Ryan, J., Althobaity, W., Gupta, A., Arribas, E., Santiago, L., Ballard, D. H., Wang, K. C., Weadock, W., Ionita, C. N., Mitsouras, D., Morris, J., Matsumoto, J., Christensen, A., Liacouras, P., Rybicki, F. J. & Sheikh, A. Radiological Society of North America (RSNA) 3D printing Special Interest Group (SIG): guidelines for medical 3D printing and appropriateness for clinical scenarios. *3D Print. Med.* **4**, 11 (2018).

[109] Ma, Z., Natal Jorge, R. M., Mascarenhas, T. & Manuel Tavares, ao R. Segmentation of female pelvic organs in axial magnetic resonance images using coupled geometric deformable models. *Comput. Biol. Med.* **43**, 248–258 (2013).

[110] Fallahi, A., Pooyan, M., Ghanaati, H., Oghabian, M. A., Khotanlou, H., Shakiba, M., Jalali, A. H. & Firouznia, K. Uterine Segmentation and Volume Measurement in Uterine Fibroid Patients' MRI Using Fuzzy C-Mean Algorithm and Morphological Operations. *Iran. J. Radiol.* **08**, 150–156 (2011).

[111] House, M., McCabe, R. & Socrate, S. Using imaging-based, three-dimensional models of the cervix and uterus for studies of cervical changes during pregnancy. *Clin. Anat.* **26**, 97–104 (2013).

[112] Yochum, M., Laforêt, J. & Marque, C. An electro-mechanical multiscale model of uterine pregnancy contraction. *Comput. Biol. Med.* **77**, 182–194 (2016).

[113] Yochum, M., Laforêt, J. & Marque, C. Multi-scale and multi-physics model of the uterine smooth muscle with mechanotransduction. *Comput. Biol. Med.* **93**, 17–30 (2018).

[114] Aluwee, S. A. Z. B. S., Kato, H., Zhou, X., Hara, T., Fujita, H., Kanematsu, M., Furui, T., Yano, R., Miyai, N. & Morishige, K. Magnetic resonance imaging of uterine fibroids: a preliminary investigation into the usefulness of 3D-rendered images for surgical planning. *Springerplus* **4**, 384 (2015).

[115] Mason, S. A., O'shea, T. P., White, I. M., Lalondrelle, S., Downey, K., Baker, M., Behrens, C. F., Bamber, J. C. & Harris, E. J. Towards ultrasound-guided adaptive radiotherapy for cervical cancer: Evaluation of Elekta's semiautomated uterine segmentation method on 3D ultrasound images. *Med. Phys.* **44**, 3630–3638 (2017).

[116] Niederer, P., Weiss, S., Caduff, R., Bajka, M., Szekély, G. & Harders, M. Uterus models for use in virtual reality hysteroscopy simulators. *Eur. J. Obstet. Gynecol. Reprod. Biol.* (2009) doi:10.1016/j.ejogrb.2009.02.009.

[117] Maneas, E., Xia, W., Nikitichev, D. I., Daher, B., Manimaran, M., Wong, R. Y. J., Chang, C. W., Rahmani, B., Capelli, C., Schievano, S., Burriesci, G., Ourselin, S., David, A. L., Finlay, M. C., West, S. J., Vercauteren, T. & Desjardins, A. E. Anatomically realistic ultrasound phantoms using gel wax with 3D printed moulds. *Phys. Med. Biol.* **63**, (2018).

[118] Pazos, V., Mongrain, R. & Tardif, J. C. Polyvinyl alcohol cryogel: Optimizing the parameters of cryogenic treatment using hyperelastic models. *J. Mech. Behav. Biomed. Mater.* **2**, 542–549 (2009).

[119] Jiang, S., Su, Z., Wang, X., Liu, S. & Yu, Y. Development of a new tissue-equivalent material applied to

optimizing surgical accuracy. *Mater. Sci. Eng. C* **33**, 3768–3774 (2013).

[120] Li, P., Jiang, S., Yu, Y., Yang, J. & Yang, Z. Biomaterial characteristics and application of silicone rubber and PVA hydrogels mimicked in organ groups for prostate brachytherapy. *J. Mech. Behav. Biomed. Mater.* **49**, 220–234 (2015).

[121] Sakaguchi, T., Nagano, S., Hara, M., Hyon, S. H., Patel, M. & Matsumura, K. Facile preparation of transparent poly(vinyl alcohol) hydrogels with uniform microcrystalline structure by hot-pressing without using organic solvents. *Polym. J.* **49**, 535–542 (2017).

[122] Hassan, C. M. & Peppas, N. A. Structure and applications of poly(vinyl alcohol) hydrogels produced by conventional crosslinking or by freezing/thawing methods. *Adv. Polym. Sci.* **153**, 37–65 (2000).

[123] Gonzalez, J. S., Maiolo, A. S., Hoppe, C. E. & Alvarez, V. A. Composite Gels Based on Poly (Vinyl alcohol) for Biomedical Uses. *Procedia Mater. Sci.* **1**, 483–490 (2012).

[124] Mix, D. S., Stoner, M. C., Day, S. W. & Richards, M. S. Manufacturing Abdominal Aorta Hydrogel Tissue-Mimicking Phantoms for Ultrasound Elastography Validation. *J. Vis. Exp.* e57984 (2018) doi:10.3791/57984.

[125] Nkhwa, S., Lauriaga, K. F., Kemal, E. & Deb, S. Poly(vinyl alcohol): Physical Approaches to Designing Biomaterials for Biomedical Applications. *Conf. Pap. Sci.* **2014**, 1–7 (2014).

[126] Jiang, S., Liu, S. & Feng, W. PVA hydrogel properties for biomedical application. *J. Mech. Behav. Biomed. Mater.* **4**, 1228–1233 (2011).

[127] Ogrodnik, P. J. The Design Process. in *Medical Device Design* 27–51 (Elsevier, 2013). doi:10.1016/B978-0-12-391942-7.00003-9.

[128] Gent, A. N., Kaang, S. Y. & Ic, D. T. *Pull-out and Push-out Tests for Rubber-to-Metal Adhesion*. (1989).

[129] Gent, A. N., Fielding-Russell, G. S., Livingston, D. I. & Nicholsont, D. W. *Failure of cord-rubber composites by pull-out or transverse fracture*. JOURNAL OF MATERIALS SCIENCE* vol. 16 (1981).

[130] Evans, J. J. & Ridge, I. M. L. *Rope and rope-like structures*. *Compliant Structures in Nature and Engineering* vol. 20 (2005).

[131] Goldstuck, N. D. 'Bowing' forces with IUD inserters in vitro: relevance to difficult IUD insertions. *Clin. Reprod. Fertil.* **5**, 173–6 (1987).

[132] Litovitz, T. A. Temperature Dependence of the Viscosity of Associated Liquids. *J. Chem. Phys.* **20**, 1088–1089 (1952).

[133] Nguyen, T. T., Biadillah, Y., Mongrain, R., Brunette, J., Tardif, J.-C. & Bertrand, O. F. A Method for Matching the Refractive Index and Kinematic Viscosity of a Blood Analog for Flow Visualization in Hydraulic Cardiovascular Models. (2004) doi:10.1115/1.1785812.

[134] Viscosity. in *Rheology Series* vol. 3 11–35 (1989).

[135] Eytan, O., Elad, D., Zaretsky, U. & Jaffa, A. J. A glance into the uterus during in vitro simulation on embryo transfer. *Hum. Reprod.* **19**, 562–569 (2004).

[136] Cheng*, N.-S. Formula for the Viscosity of a Glycerol−Water Mixture. (2008) doi:10.1021/IE071349Z.

[137] Dow. Density of Aqueous Glycerol Solutions. *Edge* 99800.

[138] Fedorov, A., Beichel, R., Kalpathy-Cramer, J., Finet, J., Fillion-Robin, J.-C., Pujol, S., Bauer, C., Jennings, D., Fennessy, F., Sonka, M., Buatti, J., Aylward, S., Miller, J. V, Pieper, S. & Kikinis, R. 3D Slicer as an image computing platform for the Quantitative Imaging Network. *Magn. Reson. Imaging* **30**, 1323–41 (2012).

[139] 3D Slicer. https://www.slicer.org/.

[140] Kenyont, N. J., Stevens+, J. C., Stewartt, P., Black+, M. M. & Clifford+, A. *A critical investigation of the measurement of the force required to dilate the human uterine cervix*. *Clin. Phys. Physiol. Meas* vol. 9 (1988).

[141] Goldstuck, N. D. & Wildemeersch, D. Role of uterine forces in intrauterine device embedment, perforation, and expulsion. *Int. J. Womens. Health* **6**, 735–744 (2014).

[142] Wang, L., Li, C., Sun, Q., Xia, D. & Kao, C. Y. Active contours driven by local and global intensity fitting energy with application to brain MR image segmentation. *Comput. Med. Imaging Graph.* **33**, 520–531 (2009).

[143] Akselrod-Ballin, A., Eyal, E., Galun, M., Furman-Haran, E., Gomori, J. M., Basri, R., Degani, H. & Brandt, A. *Automatic Three-Dimensional Segmentation of MR Images Applied to the Rat Uterus*. https://pdfs.semanticscholar.org/0187/5735a9e42a3ad62cf10bf5a348c213222efe.pdf.

[144] Asiedu, M. N., Agudogo, J., Krieger, M. S., Miros, R., Proeschold-Bell, R. J., Schmitt, J. W. & Ramanujam, N. Design and preliminary analysis of a vaginal inserter for speculum-free cervical cancer screening. *PLoS One* **12**, e0177782 (2017).

[145] Primaryteacher. https://www.interchemnet.com/newnav/Homepage/Highschool/Primary_Colors/primaryteacher.htm.

[146] Institute for Health Metrics and Evaluation. GBD Compare | IHME Viz Hub. https://vizhub.healthdata.org/gbd-compare/.

8 APPENDICES

A. SAMPLE COLLECTION PROCESS

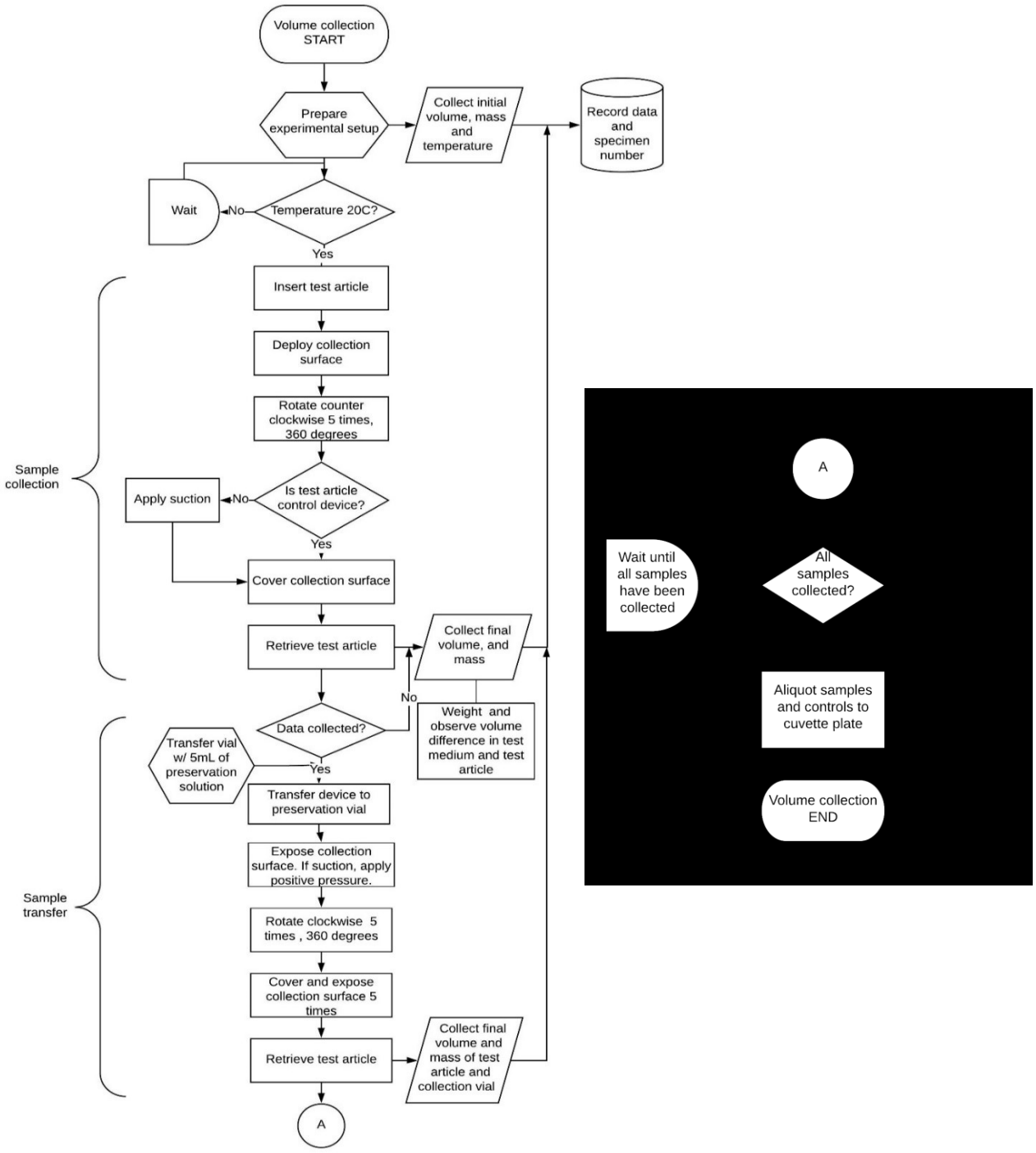

Figure 8-1 — Flowchart of sample collection for volume performance assessment.

B. OVARIAN AND ENDOMETRIAL CANCER DEMOGRAPHICS

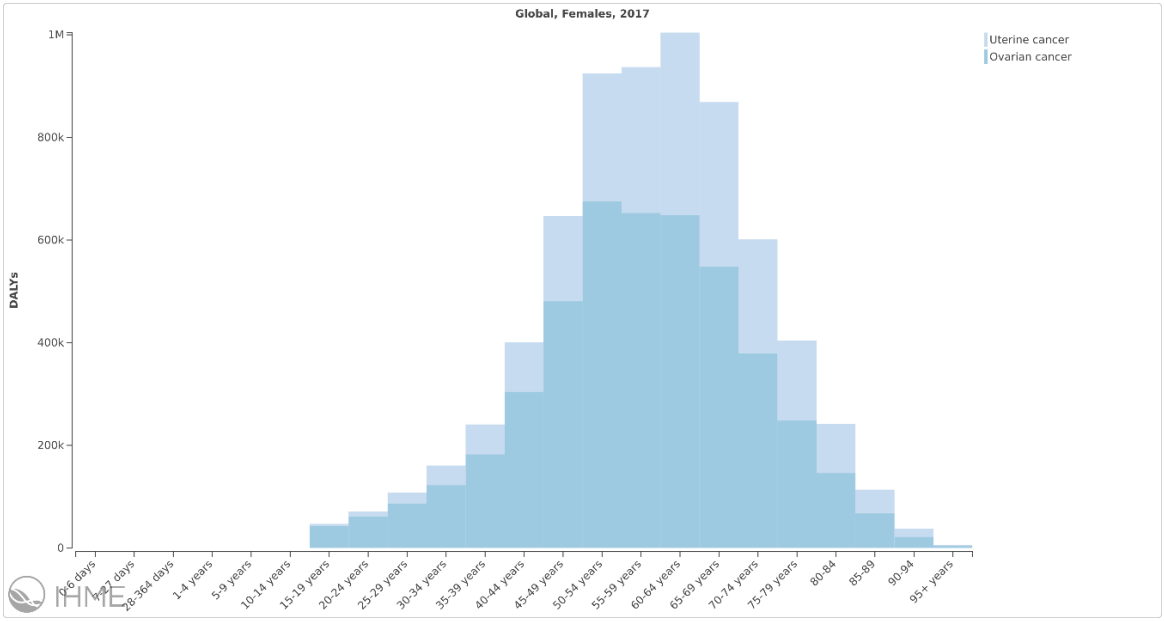

Figure 8-2 — Global Disability Adjusted Life Years (DALYs) for ovarian and endometrial cancers per age group. [146]

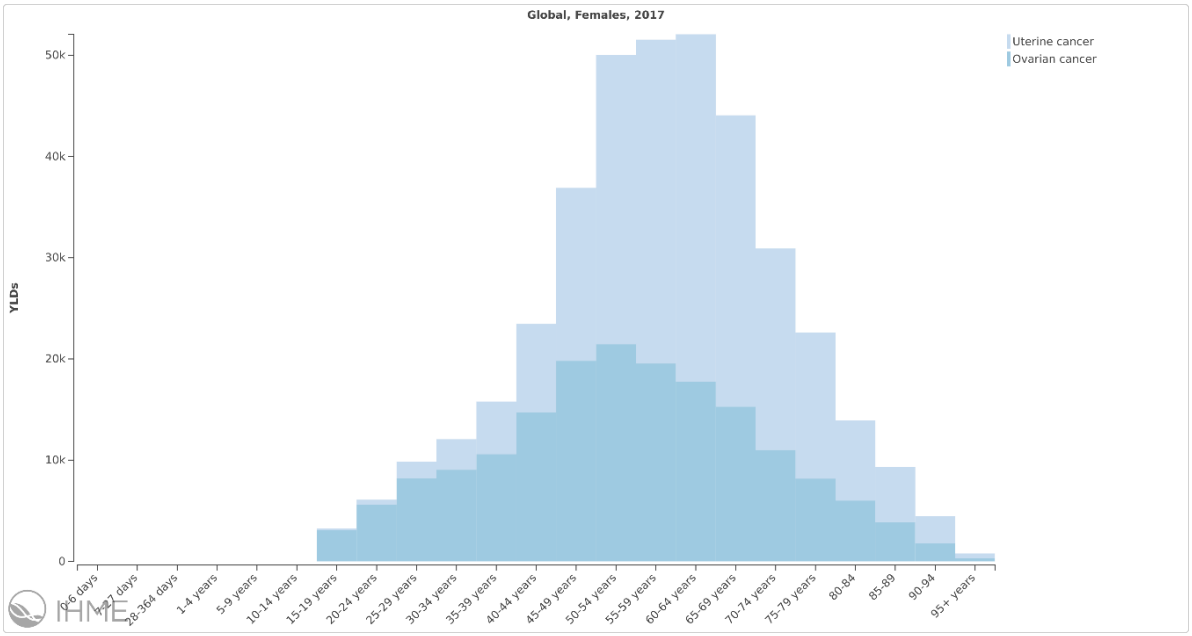

Figure 8-3—Years of Life Disabled (YLDs) for ovarian and endometrial cancers per age group. [146]

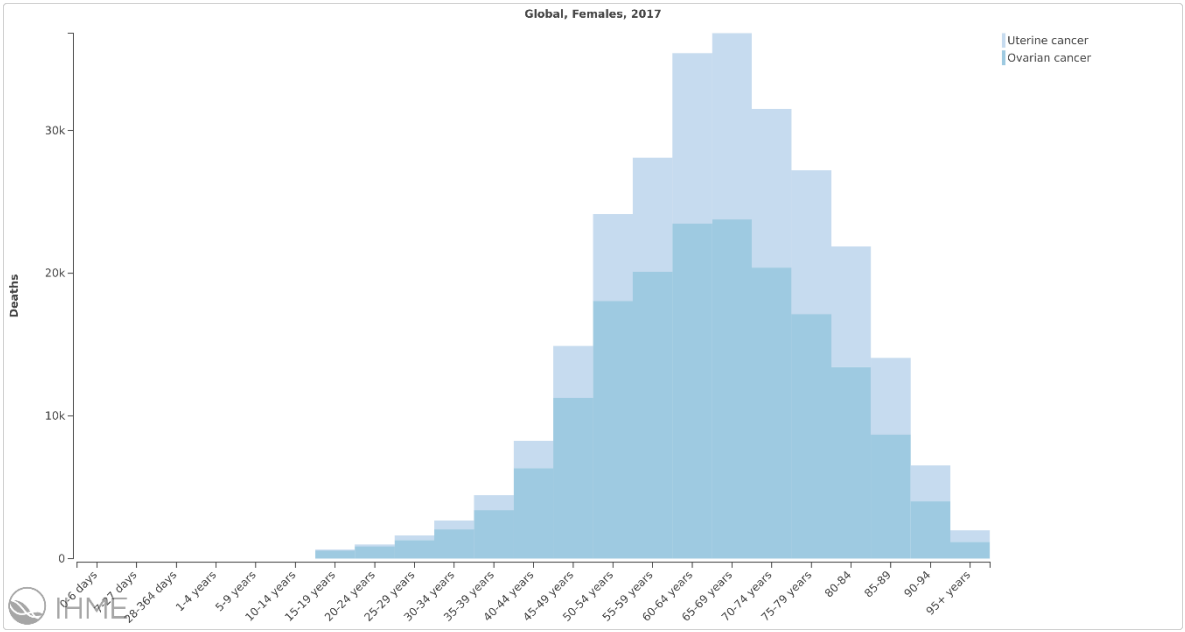

Figure 8-4—Global deaths due to ovarian and endometrial cancer in 2017 per age group. [146]

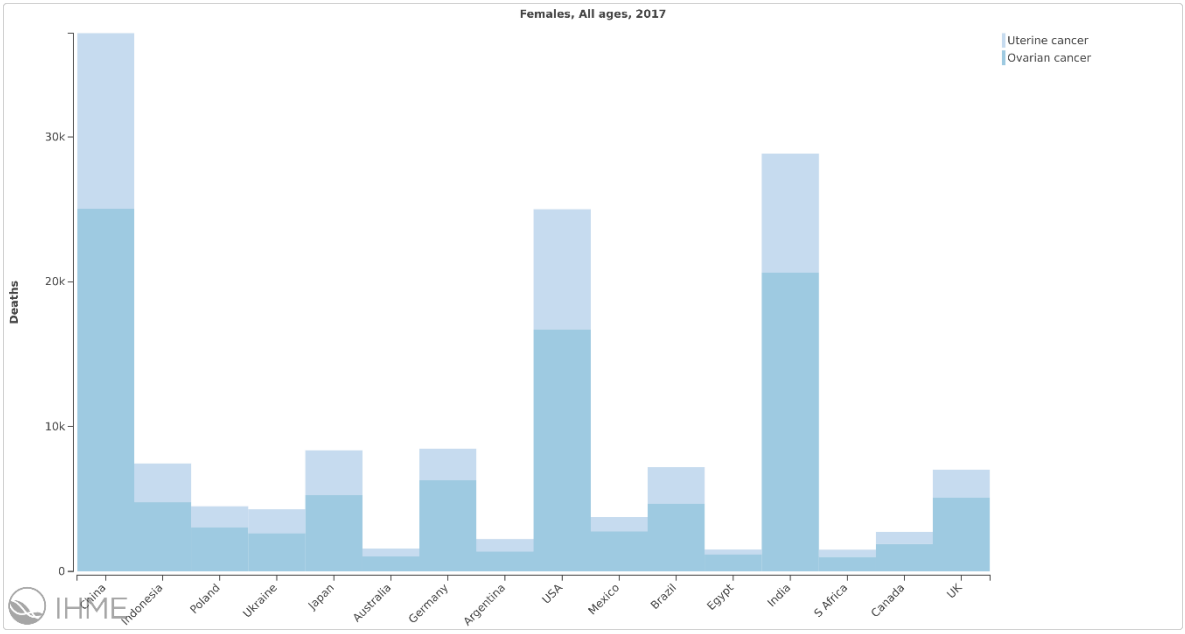

Figure 8-5—Number of deaths due to ovarian and endometrial cancers per country in 2017. [146]